2013-11-01

Dynamic Nanochannels for Biosensing Applications

Joseph B. Oxborrow
Brigham Young University - Provo

Dynamic Nanochannels for Biosensing Applications

Joseph Oxborrow

A thesis submitted to the faculty of
Brigham Young University
in partial fulfillment of the requirements for the degree of

Master of Science

Gregory P. Nordin, Chair
Brian A. Mazzeo
Adam T. Woolley

Department of Electrical and Computer Engineering

Brigham Young University

November 2013

ABSTRACT

Dynamic Nanochannels for Biosensing Applications

Joseph Oxborrow
Department of Electrical and Computer Engineering
Master of Science

Inexpensive label-free detection of biomarker panels in serum could revolutionize early cancer diagnosis and treatment. Such detection capabilities may be possible with dynamic nanochannels in conjunction with electrical impedance measurement. In Dr. Greg Nordin's lab I designed, fabricated and tested several iterations of these sensors with polydimethylsiloxane microfluidics. The final design yielded a dynamic nanochannel array sensor that showed a 140% impedance change when exposed to 14μM bovine serum albumin in phosphate buffered saline. For the geometry and noise limits of the tested device, simulations indicated that a minimum detectable concentration of 20pM with specifically bound streptavidin should be possible. However, the polydimethylsiloxane approach is also shown to be problematic in meeting the trade-offs required for a practical device. Consequently, alternative materials and designs are suggested to reduce the minimum detectable concentration to the high femtomolar range, which would be attractive for detection of many medical biomarkers.

Keywords: Proteomics, biomarkers, nanochannels, impedance sensing

ACKNOWLEDGMENTS

I would like to thank Dr. Greg Nordin for his help and guidance both in and out of the lab. I'd also like to thank my committee members: Dr. Brian Mazzeo and Dr. Adam Woolley for their input into the project. I am also very grateful for the members of the group who are my mentors and friends. I need to recognize those who fabricated the devices described in this thesis: Dr. Weisheng Hu, Tim Gustafson and Ben Tsai. I'm grateful to Dr. Stan Ness who provided guidance and pioneered the functionalization methods used, Dr. Seunghyun Kim who taught me fluid handling, Dr. Jong Noh for cleanroom training and Dr. Ryan Anderson who showed me how to run an experiment. I'd also like to thank Danny Richards for introducing me to the group as well as Chad Rogers for his patient chemistry explanations. I am deeply indebted to my family for their unwavering help and support and God who inspires in all good works.

Table of Contents

List of Tables

List of Figures

Chapter 1

Introduction

Proteomic biomarker assays hold great promise for early detection of many diseases, particularly various types of cancer [1] [2] [3]. However, this promise has not been realized due to limitations in current sensing technology. Enzyme-linked immunoabsorbent assays (ELISAs) are the gold standard for low concentration proteomic assays, but suffer because of their time intensive and expensive nature [4]. Mass spectrometry has been identified as the future leading sensor technology for sensing and identifying proteins. These machines have many advantages over ELISA but their sensitivity is limited [5] [6] [7]. Unless the sensitivity of mass spectrometry can be significantly improved a new proteomic sensing technology is needed.

Table 1.1: Cancer Survival Rates

Stage	**0**	**IA**	**IB**	**IIA**	**IIB**	**IIC**	**IIIA**	**IIIB**	**IIIC**	**IV**
Lung (non-small cell)	-	49%	45%	30%	31%	-	14%	5%	-	1%
Colorectal	-	74%	74%	67%	59%	37%	73%	46%	28%	6%
Breast	93%	88%	88%	81%	74%	-	67%	41%	49%	15%
Pancreatic	-	14%	12%	7%	5%	-	3%	3%	3%	1%

Five year survival rates for the four deadliest types of cancer [8].

In the case of cancer, early diagnosis based on improved sensing technology is critical to improving survival outcomes. The American Cancer Society estimates 159,480 deaths due to lung cancer in 2013, with the other three deadliest types of cancer estimated at 40-50,000 deaths each [8]. Table 1.1 shows survival rates for the four deadliest types of cancer according to the cancer stage at first diagnosis. Stage 0 and I cancers are localized and easier

to treat as demonstrated by the survival rates for these stages. In later stages, as the cancer metastasizes, treatment becomes increasingly difficult and survival rates drop accordingly. Early detection would cause the prognosis for thousands of patients to dramatically improve. Developing an inexpensive proteomic sensor holds the promise of widespread cancer screening and detection, enabling many more of these cancers to be successfully treated. An improved proteomic sensor could also be utilized to track cancer growth and the effects of different drugs, thereby allowing a more effective personalized treatment plan [2].

Several individual biomarkers have been found to correlate with different types of cancer [7]. However, these correlations may not be as strong as required for meaningful clinical testing. In 2006 Dalton and Friend pointed out that understanding cancer biomarkers and their complex interactions with different types of patients would take large sample sizes and extensive collaboration between cancer researchers [1]. They further noted that in many cases detection of more than a single molecule is necessary for a test to have predictive power. For example, prostate-specific antigen (PSA) is often used for prostate cancer detection. Laxman et al. showed that in addition to screening PSA levels a larger number of biomarkers could be harnessed to provide more accurate prostate cancer diagnosis [9]. Kozak et al. showed that ovarian cancer diagnosis could be improved from a receiver operating characteristic (a measure of a test's accuracy with one being perfectly predictive) of 0.833 when only using the biomarker CA125 to 0.933 when CA125 was combined with a panel of biomarkers for diagnosis [10].

There are many avenues being explored in the search for a revolutionary proteomic sensor. In conjunction with my research group, I had fabricated and tested microcantilever sensors, which were promising in many areas but gave responses lower than needed for biomarker screening [11]. During the search for a more effective protein sensor design we desired a transduction method which was simple, well understood, and didn't require the use of a labeling molecule. Keeping the sensor label-free significantly reduces the cost and complexity of operation. We chose to explore the use of dynamic nanochannels with impedance spectroscopy. Using this approach ionic conduction through a nanochannel is reduced when analyte molecules are captured by receptors attached to the nanochannel walls.

In this thesis I describe the design, fabrication, and testing of a dynamic nanochannel proteomic sensor. The fabrication was accomplished by Dr. Weisheng Hu and Tim Gustafson, while the PDMS was fabricated by Ben Tsai. Dr. Ryan Anderson programmed the LabVIEW Virtual Instruments used in testing. I bonded the PDMS to the quartz dies, designed and fabricated clamps, prepared fluids, performed sensing experiments and modeled the sensors with simulations. I present these simulations to illustrate how the dynamic nanochannel sensor should be able to detect biomarker concentrations in the picomolar range. Such a sensor would make routine cancer screening possible.

This thesis is organized as follows. In Chapter 2 I review the literature on nanochannel impedance based sensing to provide a reference point for the work described in this thesis. In addition, I present the derivation of a formula for calculating the impedance change upon monolayer biomarker attachment in triangular nanochannels.

In Chapter 3 I describe the process by which my colleagues and I went from the concept of impedance sensing to fabricating and testing a dynamic nanochannel sensor. Through this process we learned how ions behave in fluids as well as the difference between valves closing to bulk fluid flow and sealing to ionic conduction. We also built and tested many sensor designs, each increasing our knowledge of impedance sensing.

In Chapter 4 I describe a dynamic nanochannel sensor, its design, fabrication and experimental characterization. This sensor was tested with bovine serum albumin (BSA) nonspecifically bound to the nanochannel walls. The response from the sensor corresponded to BSA coverage on the sensor walls. The BSA was introduced to the nanochannels in only fifteen minutes and gave a strong response.

In Chapter 5 I look at the molecular flux at the sensors walls for the dynamic nanochannel array compared to traditional nanochannels discussed in the literature. I show that dynamic nanochannel arrays enable increased molecular flux to the sensing surfaces, thereby reducing sensor response time. Simulation results for the minimum detectable concentration for different binding kinetics is presented.

In the Conclusion I discuss future work to be done with the dynamic nanochannel sensor. I present several avenues for improving the response of the sensor which would allow detection of sub-picomolar concentrations.

Chapter 2

Background

This chapter will explore the current literature on nanochannel impedance-based sensing. The results of published impedance sensing papers are reviewed and the difficulty of providing sufficient flow in nanochannel sensors is demonstrated. Finally, an equation relating the nanochannel dimensions to the occluded cross-sectional area due to biomarker capture is derived.

2.1 Impedance sensing

Published biological channel impedance sensing originates with Kasianowicz et al. In 1996 they used a lipid bilayer membrane as a channel to determine lengths of RNA and DNA chains [12]. Later, in 2002, Saleh and Sohn fabricated a PDMS nanochannel and detected DNA with impedance measurements [13]. With this DNA detection method a range of impedance sensors appeared that are called nanopore sensors [14] [15]. These nanopore sensors work primarily with DNA and measure the impedance through a pore to determine the DNA sequence as it passes through. There are still many challenges with these sensors such as controlling the time of flight (TOF) through the nanopore, being able to resolve different base pairings, and fabricating large arrays of nanopores. However, this sensor technology is promising in the search to enable inexpensive genome sequencing [16]. In addition to the work done with nanopores some groups use nanochannels for similar TOF calculations by placing the electrodes perpendicular to the nanochannel and detecting the change in conductance as DNA transverses the length of the nanochannel [17] [18].

Some work in impedance spectroscopy has focused on detecting changes on the electrode surfaces upon biomarker attachment [19]. However, the ionic reactions taking place on the surface of an electrode in serum are complex and not well understood such that it is

difficult to use this as the basis for a stable, high sensitivity sensor. Instead, in this thesis I consider impedance change in nanochannels through the mechanism of reduced conducting cross sectional area as molecules that are taken up on the sidewalls partially block the channel. As discussed later, high ionic concentrations in solutions allow nanochannel conduction effects to dominate [20] [21].

Though nanopore impedance sensors are well established in genomics [16], the investigation of nanochannel sensors in proteomics has been limited. In 2004 Stein et al. reported surface effects in nanochannels during ionic impedance sensing [22]. In 2005 Karnick et al. used these effects to detect streptavidin binding to biotin-coated nanochannels [20]. They explored the relationship between buffer concentration and conductance. They found the conductance tracked well with the calculated bulk conductance until surface effects dominated at lower ionic concentrations. Modifying the surface of the device with (3-aminoproypyl)trimethoxysilane (APTMS) and later sulfosuccinimidyl 2-(biotinamido)-ethyl-1,3-dithiopropionate (Sulfo-NHS-SS-Biotin) changed the conductance at lower ionic concentrations but left conductance with higher ionic concentration buffer unchanged. This concentration dependence suggests these nanochannel surfaces are charged and exhibit ionic transport but that this effect is dominated by bulk conductance at higher concentrations (higher than 10mM PBS for their system). Other groups confirmed their results [21]. Karnick et al. detected streptavidin in nanochannels. However, due to the small cross sectional area of the nanochannels (their height was 30nm) it took 10 hours to introduce a 16μM streptavidin solution to their device [20].

Schoch el al. worked on a nanochannel sensor with induced flow to decrease the time required to introduce biomarkers to the nanochannels [23]. Like Karnick et al., they biotinylated the nanochannel surfaces and detected specifically bound streptavidin. Their primary contribution was exploring the link between response time and fluid velocity in nanochannel sensors. They calculated with the diffusion constant of streptavidin and length of the channels that at velocities above 3.1 mm s^{-1} some of the analyte may flow through without attaching to the sensor walls. They also calculated that the shear forces at those speeds could be enough to break the biotin-streptavidin bond. They introduced fluid by

applying pressure with an external pump and tested velocities up to 22.9 mm s^{-1}. They were able to detect 1nM streptavidin in under two hours in their nanochannel sensors [23].

Durand et al. also built a nanochannel sensor. Instead of working with the biotin-streptavidin system they used nonspecific BSA binding. They reported an electrical model of the nanochannel sensor, explored how the impedance changed with frequency and discussed the relationship between the pH of the buffer solution and the nanochannel conductance change upon protein attachment. Their device seemed to be able to detect 600nM BSA binding to the sensor walls, with flow times just over 10 minutes [24].

Afanasiev et al. have also reported a nanochannel impedance sensor. Their sensor is based on complementary metal oxide semiconductor (CMOS) fabrication technology which would make it easy to fabricate. However their nanochannel sensors are diffusion limited as they are open on only one end. In addition the protein sensing capabilities of these sensors is not yet confirmed [25]. Ali et al. also explored building an asymmetric nanochannel sensor and saw some I-V curve changes on the introduction of 100 nM BSA to the sensor [26].

Escosura-Muñiz and Merkoçi built probably the most complete nanochannel impedance sensors. They have demonstrated detection of the cancer marker CS15-3 in whole blood. The nanochannels are fabricated in anodized aluminum oxide after which they are functionalized for the antigen or the IgG. Their approach sacrifices label-free detection by using gold nanoparticles for signal amplification but these labels allow detection of 50 ng mL^{-1} CA15-3 and 2 μg mL^{-1} of human IgG. They estimate a 50 ng mL $^{-1}$ (330 pM) detection limit for the human IgG [27].

DNA is considerably easier to detect with nanochannels than proteins due to its comparably large size. Nevertheless, protein nanochannel sensing has been demonstrated even in whole blood. Here we seek to improve the detection limits and response time compared to reported nanochannel impedance sensors. This improvement will be accomplished by increasing analyte flow to the surface and thereby decreasing the time needed to attach a specified number of biomarkers to sensor surfaces.

2.2 Nanochannel impedance derivation

This derivation is presented to enable easier calculations of detection limits and expected impedance change for a given sensor geometry and thickness of attached biomarker.

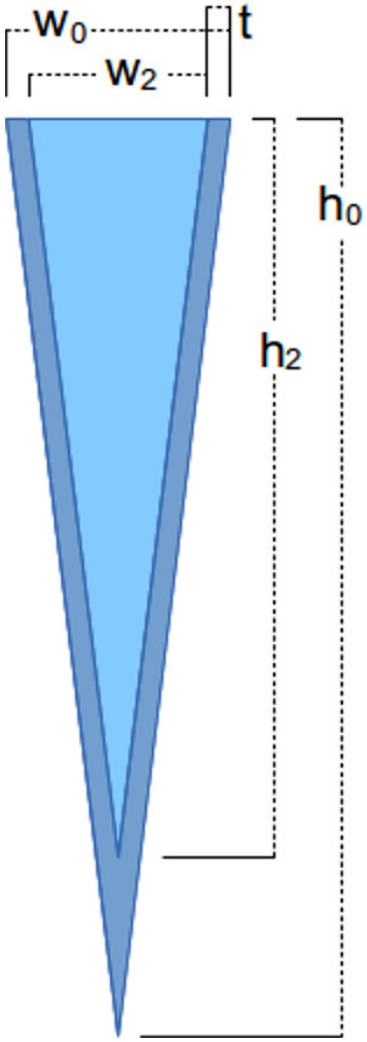

Figure 2.1: Area change of focused ion beam (FIB) milled nanochannels on biomarker attachment.

By taking the cross sectional area of a triangular nanochannel with a width w_0 and a height h_0 and applying a layer of biomarkers causing some ionic occlusion of thickness t, the percent impedance change can be calculated compared to a final width w_2 and final height h_2 (see Fig. 2.1). The initial cross sectional area is given by

$$area_0 = \frac{w_0 h_0}{2}, \tag{2.1}$$

and final by

$$area_2 = \frac{w_2 h_2}{2}. \tag{2.2}$$

The percent impedance change is calculated by taking the final impedance minus the initial impedance divided by the initial impedance

$$\Delta\Omega = \frac{\Omega_2 - \Omega_0}{\Omega_0}, \tag{2.3}$$

or

$$\Delta\Omega = \frac{\frac{2l}{\sigma w_2 h_2} - \frac{2l}{\sigma w_0 h_0}}{\frac{2l}{\sigma w_0 h_0}}. \tag{2.4}$$

The initial width is related to the final width by subtracting twice the thickness of the occluded layer

$$w_2 = w_0 - 2t, \tag{2.5}$$

the final height is then

$$h_2 = \frac{h_0 w_2}{w_0} = \frac{h_0(w_0 - 2t)}{w_0}. \tag{2.6}$$

After plugging in variables and simplifying the equation we obtain is

$$\Delta\Omega = \frac{w_0^2}{(w_0 - 2t)^2} - 1. \tag{2.7}$$

This result is illuminating because as long as h_0 is much larger than t the impedance change depends primarily on the difference between w_0 and 2t. The BSA molecules we use in our experiments are believed to have an ellipsoidal structure with minor axis $34\mathring{A}$ long and the other axes both being $84\mathring{A}$ long [28]. If the occluded thickness of a protein layer is $w_0/20$ then the impedance change will be 23%. With a layer $w_0/10$ thick the impedance change will be 56%.

Chapter 3

Design and Fabrication Process

3.1 Interdigitated electrodes

In this chapter I discuss the series of designs that eventually led to the development of dynamic nanochannels for biosensing. The process began with microfabricated interdigitated electrodes placed in static PDMS flow channels. These first sensors gave inconsistent results. My research group and I determined that the conduction through the fluid above the interdigitated electrodes dominated conduction between the electrodes, thereby preventing consistent impedance changes where bacteria or biomolecules were captured between electrode fingers. With this understanding we positioned valves over the interdigitated electrodes. When the valve membrane collapses on top of the electrodes, the conduction path is limited to any fluid trapped between adjacent electrode fingers. Finally, we abandoned interdigitated electrodes and put microchannels or nanochannels under the valves; this evolved into the dynamic nanochannel design that is discussed in Chapter 4.

To accomplish the goal of impedance sensing for biomolecules we first fabricated interdigitated electrodes. Instead of using impedance changes occurring on the surface of the electrodes as has often been done [19] we wanted to examine changes in the ionic paths between the electrodes. We started with interdigitated electrodes because they had the advantage of being simple and we could quickly integrate them with our current generation of PDMS designs. We postulated that the small volume between electrode fingers closest to the substrate surface would provide a significant fraction of the conduction between electrodes. Therefore the goal of the interdigitated electrode design was to trap biomolecules on the surface between electrodes to reduce the volume of fluid closest to the substrate surface between the fingers by the capture of whichever type of biomolecule for which we functionalized the substrate surface.

3.1.1 Interdigitated electrodes in PMDS flow channels

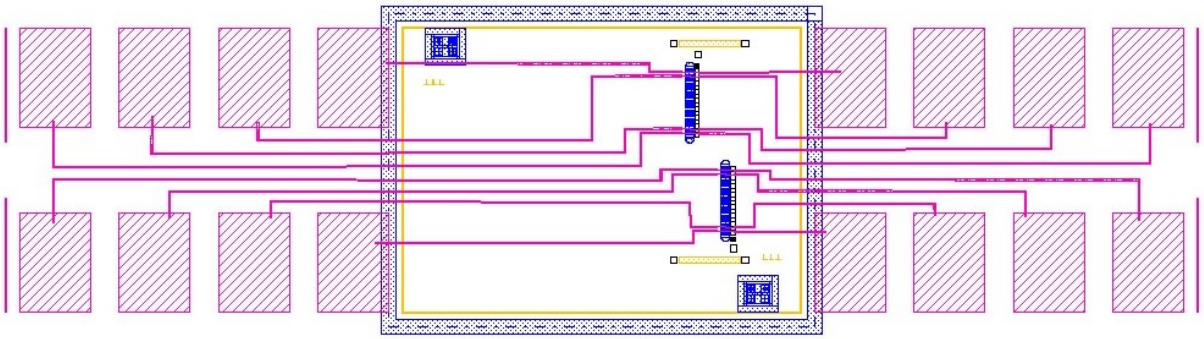

(a) Schematic of Interdigitated Electrode Mask.

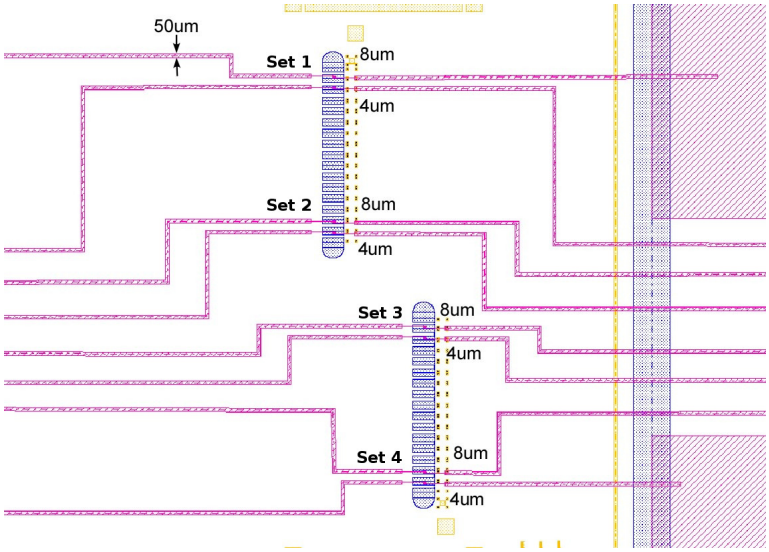

(b) Die level close-up.

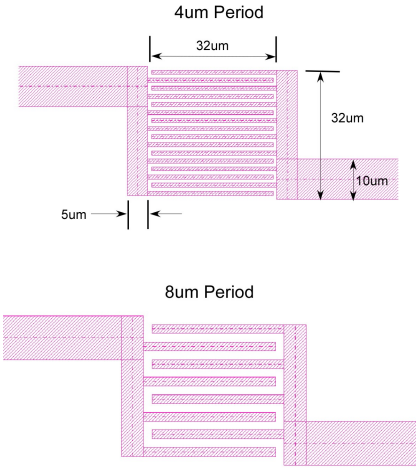

(c) Close-up of an electrode set.

Figure 3.1: IDE schematics.

Our group had previously used microcantilevers for biosensing. As a starting point, we took the PDMS layout we had designed for the microcantilever experiments and re-purposed it for interdigitated electrode sensing runs. The height of the first electrode die stayed the same as the microcantilever dies (1.2cm) but the width was expanded to 4cm (see Fig. 3.1a). The microcantilever die had two microcantilever arrays. On the interdigitated electrode die in these two areas two sets of interdigitated electrodes were placed (see Fig. 3.1b). We fabricated two electrode designs in each set; one with 2μm lines and spaces and

the other with 1μm lines and spaces. Both designs had areas of 32μm x 32μm (see Fig. 3.1c). Each set was numbered one through four, with one being closest to the top of the die as oriented in Fig. 3.1b. Electrodes one and three have 1μm lines and spacings while electrodes two and four have 2μm lines and spacings. Fabricated electrodes are shown in Fig. 3.2a.

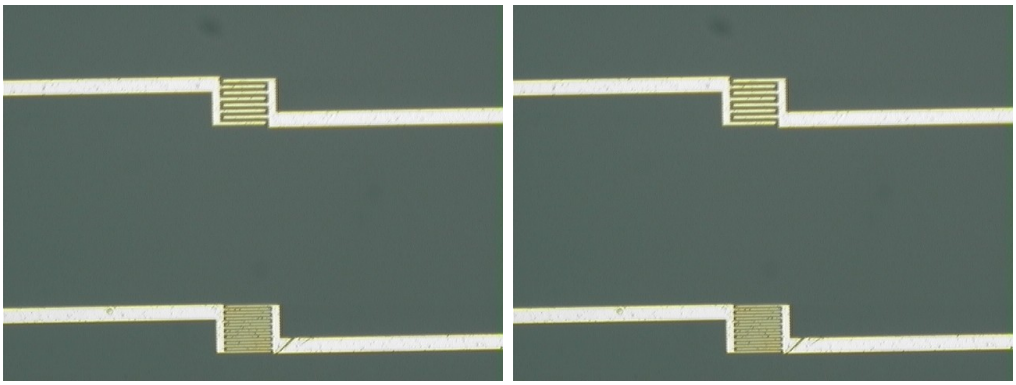

(a) Microscope photo of fabricated IDE.

(b) Microscope photo of fabricated IDE functionalized with CSA.

Figure 3.2: Fabricated IDEs.

Fabrication

There were several versions of interdigitated electrodes fabricated before we arrived at the sensor described in chapter 4. These designs used a similar fabrication process to the one described below, although with different masks and die sizes.

First, a 100mm quartz wafer is dehydration baked in an oven at 150°C for 10 minutes. After baking, an adhesion promoter, Surpass 4000 is spun on at 4000 rpm for one minute. Next AZ2020 photoresist diluted 1:1 with propylene glycol methyl ether actetate (PGMEA) is spun on at 2000 rpm for one minute then at 6000 rpm for two seconds. The photoresist layer is then softbaked at 110°C for three minutes. UV exposure is performed for twelve seconds in a Karl Zuess Mask Aligner (MA 150CC) at 6 mW/cm^2 in vacuum contact mode. MIF3000 in a 2:1 mixture with deionized (DI) water is then used to develop the photoresist for about eleven minutes. Next, the wafer is rinsed with DI water, and an oxygen descum

is performed in a LF001 Plasma Barrel Etcher at 100W for 45 seconds. A 110nm layer of aluminum is deposited on the wafer using a Denton Vacuum E-beam evaporator. A lift-off step is then performed with acetone in an ultrasonic bath. As a protective layer during dicing, Surpass 4000 is spun on at 4000 rpm for a minute and AZ3330 at 4000 rpm also for a minute. A soft bake is performed at 90°C, then the wafer is diced into dies and finally the dies are cleaned with acetone and isopropyl alcohol (IPA).

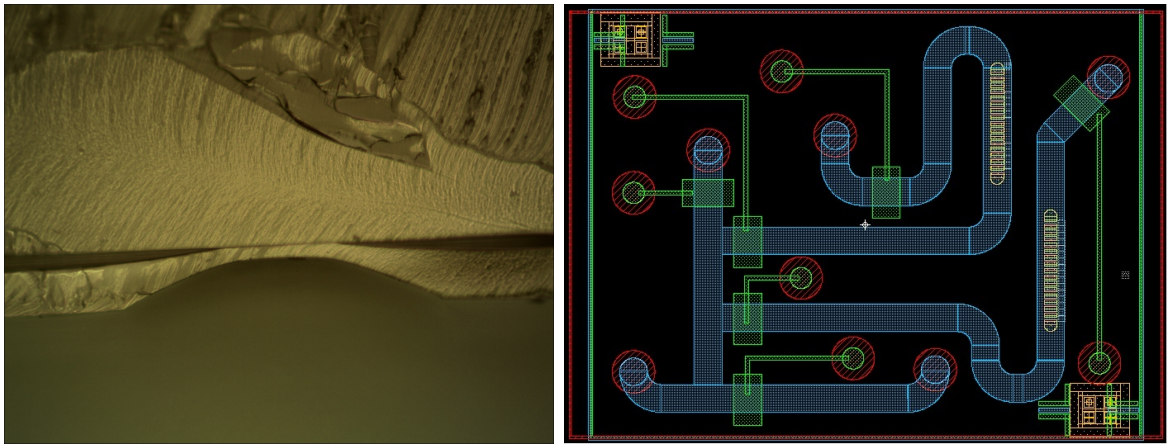

(a) Microscope image of the cross section of a fabricated PDMS flow channel. The thickness of the bottom membrane layer at the center of the microchannel is 30μm.

(b) Image of PDMS mask used with the IDE dies. This PDMS design was recycled from the microcantilever experiments and shows microcantilever sets instead of electrodes.

Figure 3.3: IDE PDMS mask and fabricated PDMS cross section.

The PDMS was fabricated in two layers: the fluidic layer and the control layer. The fluidic layer is situated between the PDMS control layer and the quartz die underneath (see Fig. 3.3a). The fluidic layer contains the microfluidic channels (blue areas in Fig. 3.3b). The control layer is situated on top of the fluidic layer and houses the control lines and valves (green areas in Fig. 3.3b).

The fluidic layer is fabricated on a 100mm silicon wafer. The silicon is first dehydration baked at 150°C for 15 minutes. Hexamethyldisilazane (HMDS) is then evaporated as a photoresist adhesion layer onto the wafer surface for 15 minutes, followed by spin coating AZ50XT photoresist onto the wafer at 900 rpm for 60 seconds giving an initial thickness of

60μm for the fluidic mold. A soft bake is performed at 60°C for 10 minutes and then 125°C for 3 minutes. The wafer is then left to hydrate in air for one hour. A hard contact exposure is performed with the Karl Zuess Mask Aligner for 60 seconds. The fluidic mold is developed for 6 minutes and 40 seconds in AZ-421K, 15 minutes in AZ-400K at a 1:3 dilution with deionized (DI) water and 40 minutes in AZ-400K at a 1:4 dilution. After a reflow bake at 125°C for 3 minutes a mixture of 10:1 PDMS to curing agent (Sylgard 184, Dow Corning Corp) which has been degassed for an hour is spun onto the wafer at 750 rpm for 80 seconds giving a thickness of 12 μm. The PDMS is then cured by baking for an hour at 80°C.

To fabricate the control layer mold SU8-2025 photoresist is used. A wafer is dehydration baked and HMDS is applied as with the fluid layer process. SU-2025 is then spun onto the wafer at 500 rpm for 6 seconds and then 4000 rpm for 30 seconds giving a photoresist thickness of 24μm. A 4:1 mixture of PDMS to curing agent is degassed for an hour. The PDMS mixture is then poured onto the wafer. The control layer is then baked at 80°C for an hour resulting in a thickness of 2.1mm.

Finally, the control layer pieces are cut from the wafer, stamped with curing agent, and bonded to fluidic layer pieces. The two layer PDMS piece is then stamped with curing agent again and bonded to the quartz die as explained in [29]. The curing agent bonding process can be accomplished with time and/or heat, ranging from leaving the pieces overnight to placing on a hot plate at 90°C for 30 minutes .

Characterization

The first tests of the interdigitated electrodes were done primarily to characterize the devices, enable us to develop a sensing protocol, and introduce us to the challenges associated with impedance sensing. Accordingly, we ran the first sensing tests with bacteria. We chose bacteria primarily for their large size in comparison to biomolecules and because they could be resolved in an optical microscope allowing us to quickly check if they had bound on the substrate surface between the electrode fingers. This gave us an additional check to see if the impedance scans were behaving as expected.

The electrodes were functionalized for the bacteria by pipetting six drops of CSA-121, a molecule which was being developed in Dr Paul Savage's lab to specifically attach

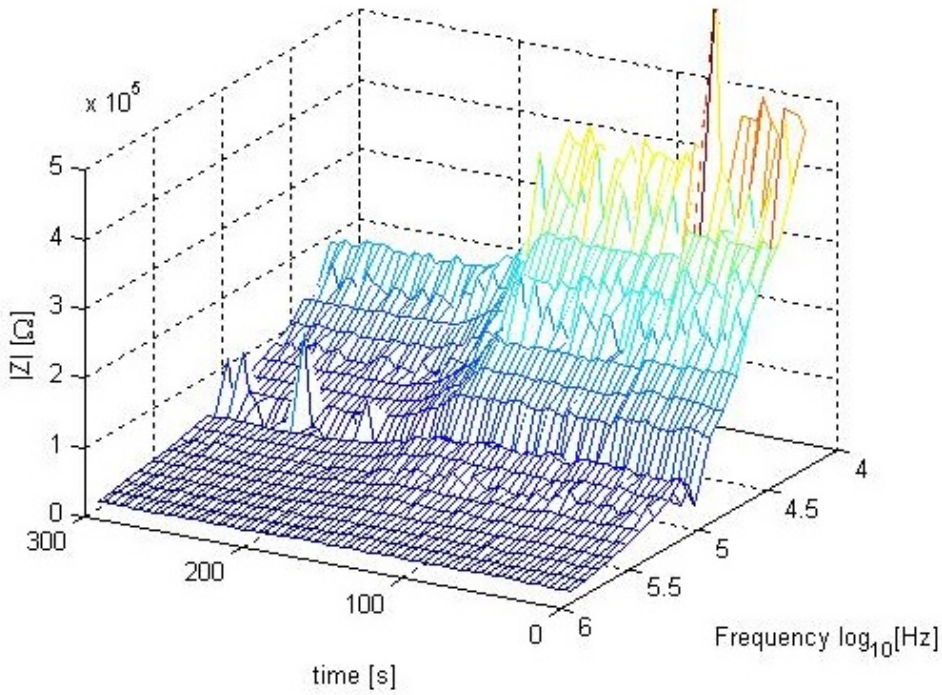

Figure 3.4: Measured impedance plotted as a function of frequency and time. The experiment begins with DI water in the channel above the IDEs. At 60 seconds the channel valve opens, at 120 seconds the syringe pumps starts, at 240 seconds pumping stops, and finally at 270 seconds the valve closes.

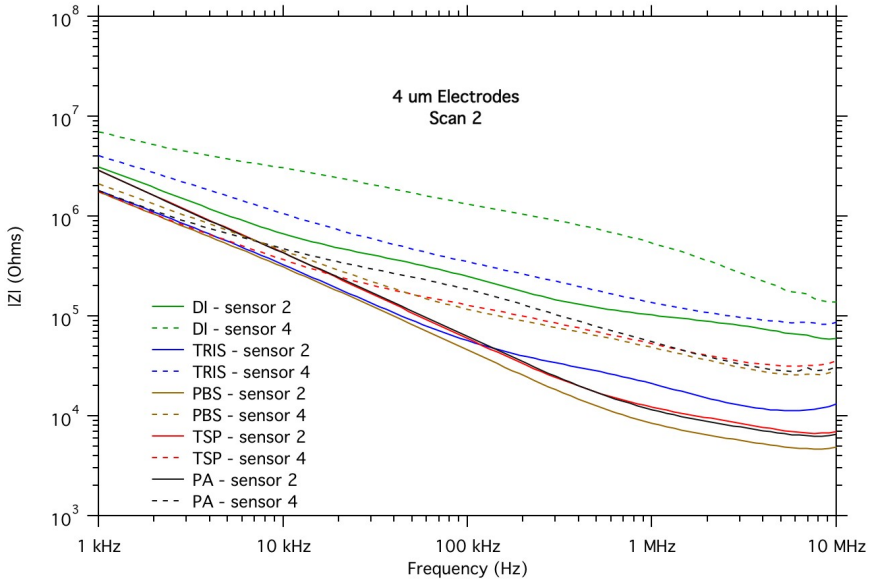

Figure 3.5: Results of a sensing experiment with DI water, buffer solutions (Tris & PBS), growth medium (TSP), and bacteria (PA).

to the bacteria, over the electrode regions (see Fig. 3.2b). PDMS was then bonded to the wafer surface. The fluidic channels were filled with DI water and continuous scans were taken as buffer solution was flowed into the channel. The higher ion content in the buffer solution is evident around 150 seconds when the buffer has flowed over the electrodes and the impedance has decreased (see Fig. 3.4). Single scans of impedance versus frequency in two buffer solutions tris(hydroxymethyl)aminomethane (Tris) and phosphate buffered saline (PBS), in tryptic soy broth, and finally impedance scans were taken with bacteria flowing through the channel (see Fig. 3.5). After several experiments it was clear that having the bacteria attach to the CSA-121 in flowing fluid wasn't likely and when a binding event did appear to happen we weren't able to detect it. In Fig. 3.5 there is an example of the results from this series of experiments. The red traces indicate impedance of the growth medium prior to bacteria introduction while the black traces are with bacteria flowing through the channel. The traces diverge only slightly for sensor 4 (dashed lines) around 100kHz while for sensor 2 (solid lines) they look almost identical.

This design didn't seem to be able to detect the comparatively large bacteria in open channels. We reasoned the electric fields might be less concentrated between the electrode fingers than we previously thought. An experiment taking impedance scans while increasing the size of a droplet of PBS buffer solution above the electrodes showed the conductance increasing almost linearly with droplet diameter. This experiment suggested the importance of conductance paths through the top surfaces of the electrodes and fluid above the electrode fingers. Zou et al. using finite element analysis software modeled the electric field strength around interdigitated electrodes in fluid [30] which also suggested the relative importance of the conduction paths through the top surfaces of the electrode fingers.

3.1.2 Interdigitated electrodes with PDMS valves

After the disappointing results with the IDEs in open channels and seeing the importance of the conduction through the volume above the electrodes we designed an innovative valve closing method to concentrate the electric field lines between the electrode fingers (see Fig. 3.6). Four extra valves were added to the PDMS design; each valve over one set of electrodes. When the valves actuated the PDMS would collapse around the IDEs. The

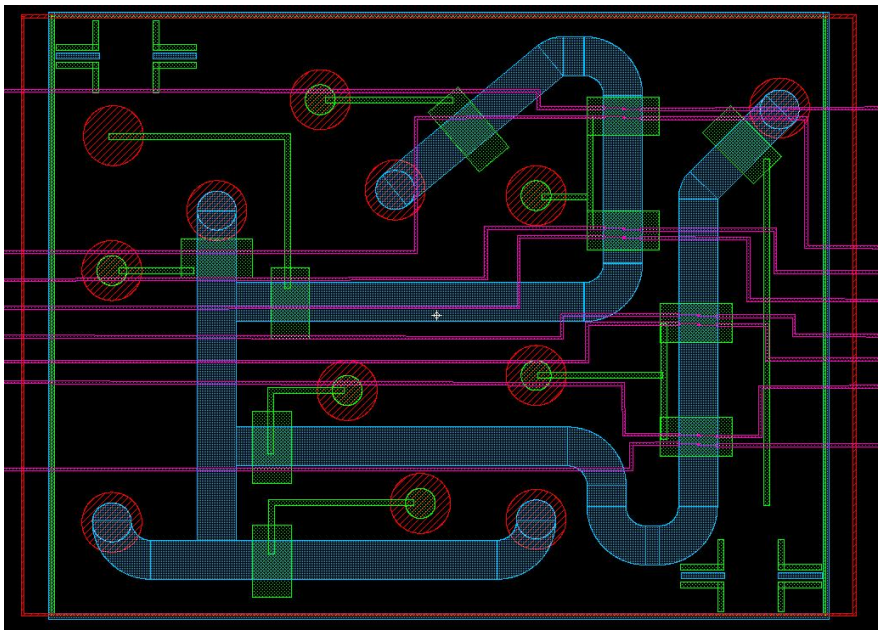

Figure 3.6: Image of PDMS mask used with the IDE dies, this PDMS fluidic layer (in blue) design was recycled from previous iteration but has valves (in green) above the electrodes.

actuation pressure would determine the degree of PDMS conformation onto the IDE fingers. When a light pressure was applied the PMDS would lightly press against the electrodes while at the maximum pressure (around 30PSI) the PDMS would collapse much of the way into the gaps between the electrode fingers. With the PDMS valves actuated onto the electrodes at high pressures the fluid conduction path would be solely between the electrode fingers allowing the biomolecules to impede a much larger portion of the conduction path.

In order to characterize these valves we ran a couple preliminary experiments. We expected the volume of conducting fluid between electrode fingers would depend on the pressure applied to the valve. This led us to run an experiment where we took impedance scans as we varied the valve pressure from 2 to 5, 10, 20, and 30PSI with a 40mM Tris buffer (see Fig. 3.7a) as well as a 250mM PBS buffer (see Fig. 3.7b). The results from the two buffers looked similar. Without pressure being applied to the valve the impedance was low, after application of pressure the impedances steadily increased until 20PSI at which point the PDMS valve appears to have almost reached its limit in conforming around the electrodes; increasing the pressure to 30PSI only slightly affected the impedance. Taking a scan in air and looking at the lowest frequency queried (1kHz) the impedance is around $10^9 \Omega s$, however

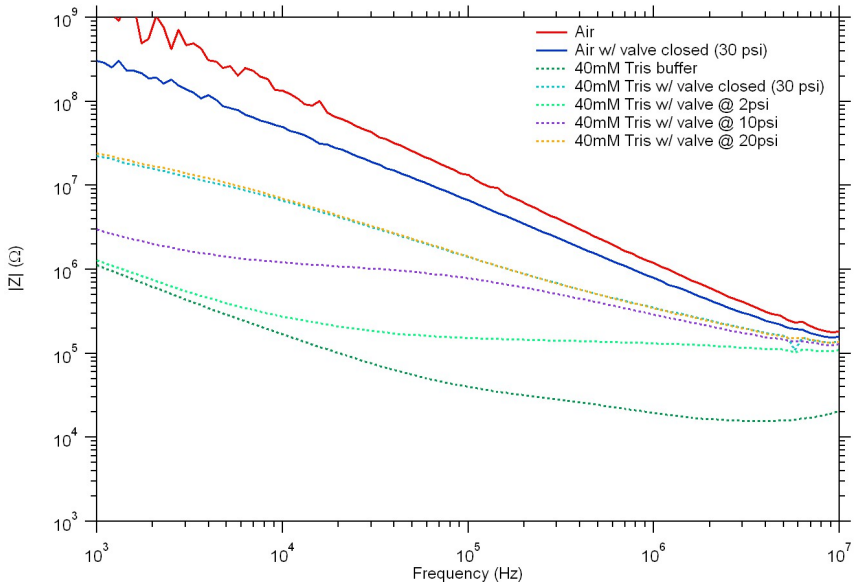

(a) Pressure ramps with 40mM Tris solution.

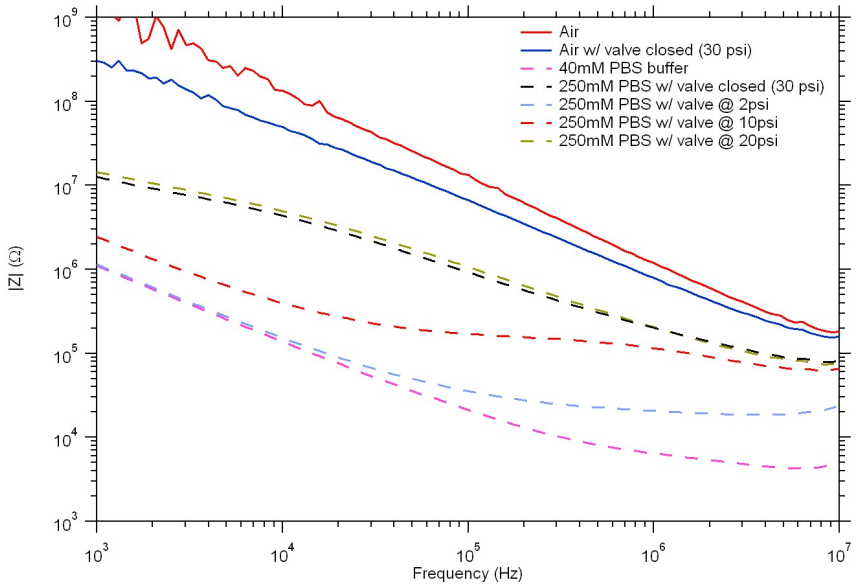

(b) Pressure ramps with 250mM PBS solution.

Figure 3.7: Pressure ramps with Die Q8 showing increasing impedance with increased pressure.

at 30PSI for both buffers the impedance is slightly over $10^7 \Omega s$. This impedance suggests the PDMS valves do not collapse completely into the channels but leave a conduction path useful for biomolecular sensing.

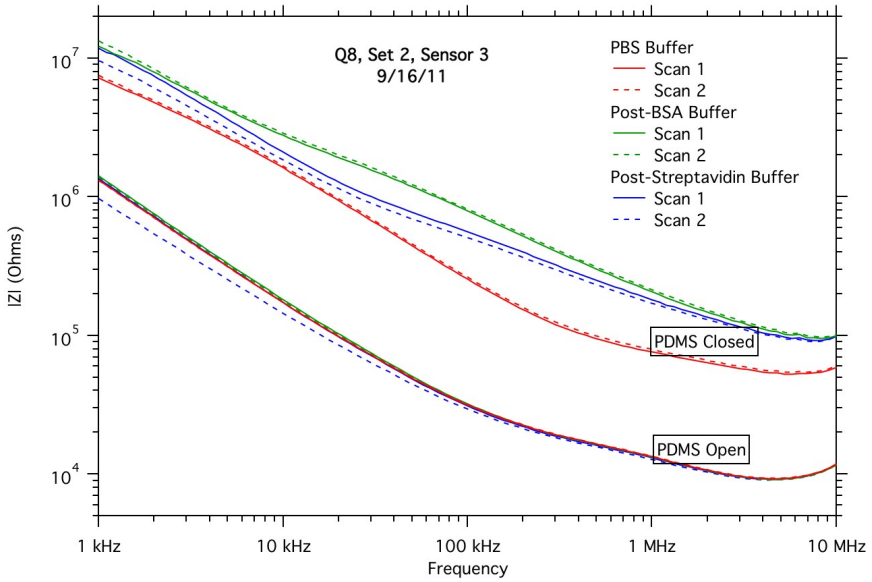

Figure 3.8: Results of sensing runs with Q8; the valve was closed at 30PSI, both BSA and streptavidin are 17μM solutions.

After characterizing the valves we ran a series of sensing experiments. We started experimenting with bacteria but it wasn't clear if with their size they should impede conduction paths, behave like tent poles propping up the PDMS valve, or rupture when pressed with the PDMS valve. After brief experiments working with bacteria the data was inconclusive so we turned to a protein system we had worked with before: biotinylated BSA and streptavidin.

The new protocol for sensing required taking scans in air before the introduction of fluid after which buffer is flowed into the channels. Next, open and closed scans at 30PSI are taken (PBS Buffer), biotinylated BSA is then introduced to the channels and a buffer rinse is performed. After the rinse, open and 30PSI scans are taken (Post-BSA Buffer), streptavidin is then flowed into the channels, a buffer rinse is performed, and the final set of scans are taken (Post-Streptavidin Buffer) (see Fig. 3.8).

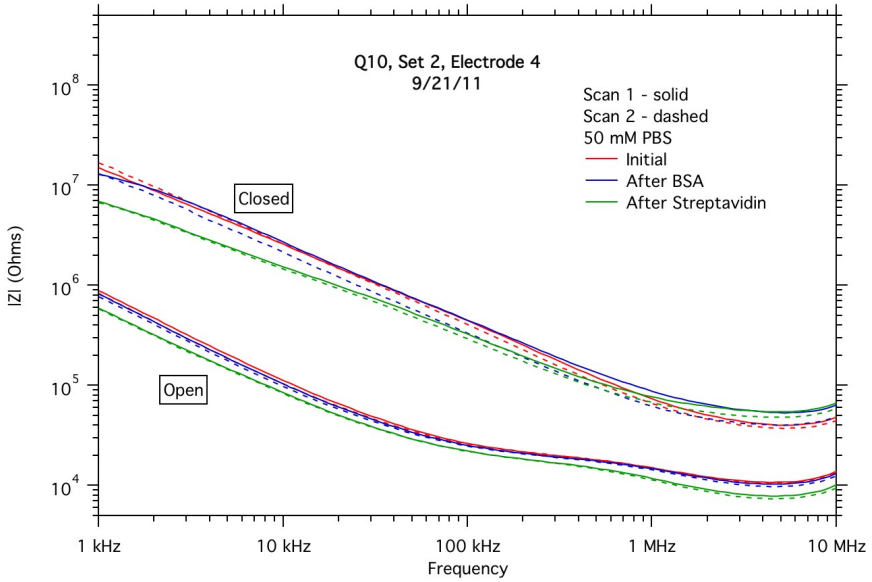

Figure 3.9: Results of sensing runs with Q10; the valve was closed at 30PSI, both BSA and streptavidin are 17μM solutions.

One electrode from one of the dies gave a promising result (see Fig. 3.8) but the majority of the results didn't look so promising (see Fig. 3.9 for example). Scans on Die Q10 for buffer (Initial) and for BSA look quite similar in open and closed situations while the results with streptavidin show slightly decreased impedance compared to the other two. Perhaps the streptavidin results could be useful except for two things: first, the impedance should increase not decrease as the biomolecules impede conduction between electrode fingers and second, the results are inconsistent between experiments (see Fig. 3.14 for a case when impedance increases with streptavidin). With the idea that these sensors could and should work we went looking for the sources of our often conflicting results.

One of the first places we looked was at PDMS valve placement. By the nature of the valve design and alignment error, the electrodes were seldom directly centered under the valve membrane; a typical placement is shown in Fig. 3.10. Although one of the better alignments the center of the valve is only centered above the 2^{nd} and 3^{rd} electrodes. We noticed an electrode which gave promising results appeared to be particularly well aligned under the valve. So we focused on valve placement to see if this was the source of variability. However, we found that many of the electrodes where placement looked particularly good had inconsistent results.

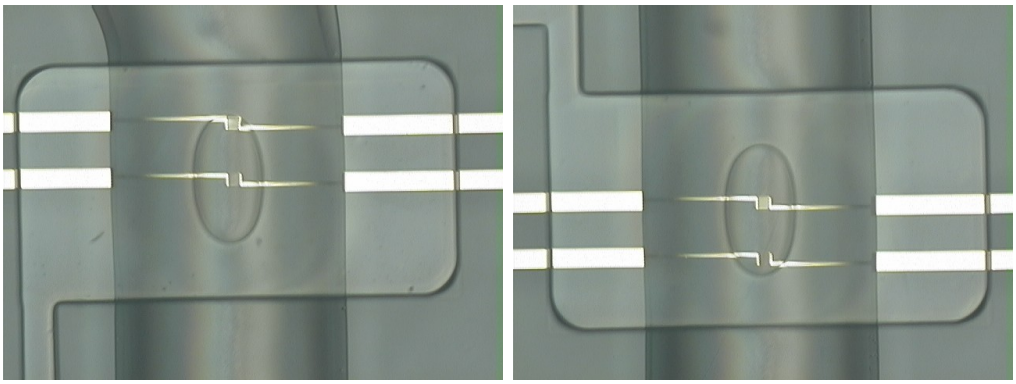

Figure 3.10: Q10 Set 1 electrodes under PDMS.

The next suspect in our hunt for the source of the inconsistent results was electrode thickness. Perhaps the PDMS valves were in many cases sealing off in between the valves and giving results which didn't seem to depend on the bound molecules (see Fig. 3.9). To this end the electrodes were deposited to a greater thickness of 220nm and we tried electroplating them to an even greater thickness. After running more tests this also seemed to be of no avail.

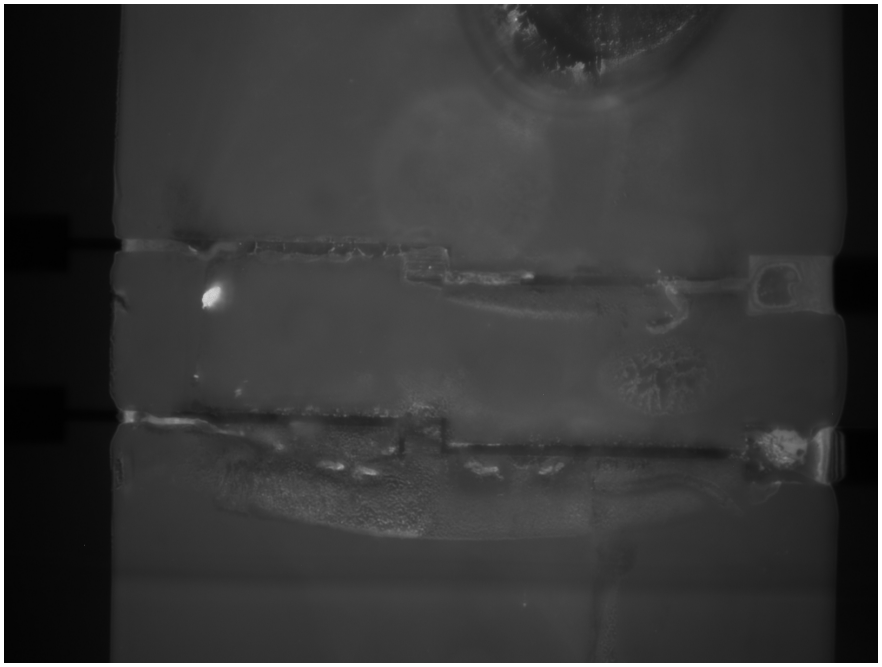

Figure 3.11: Fluorescence image of Q10 Set 2 electrodes 1&2 after the sensing run.

Finally we began to suspect the curing agent used in the PDMS fabrication and as the bonding agent between the quartz substrate and the PDMS fluid layer. Fig. 3.11 is a fluorescence image of one of the dies after a sensing run. The streptavidin had a fluorescent tag allowing us to examine where the streptavidin had bound. In examining one of these images we noticed a thick film above the electrodes which was broken in places. In Fig. 3.11 we see the thick layer folded above the electrode lines on the left side of both the electrode lines. This film seemed too thick to consist of the BSA and streptavidin so we suspected it was curing agent contaminating the surface during the bonding process. The PDMS is stamped on a wafer which has been spun with a thin layer of curing and then is aligned and placed on the quartz die. After placement, curing agent is heat cured at 70°C for 30 minutes then at 90° for another 30 minutes. We postulated the heat cure volatilized the curing agent and it redeposited in the electrode region or the curing agent had an affinity for the gold surfaces of the electrodes and wicked across them sometime during the bonding process.

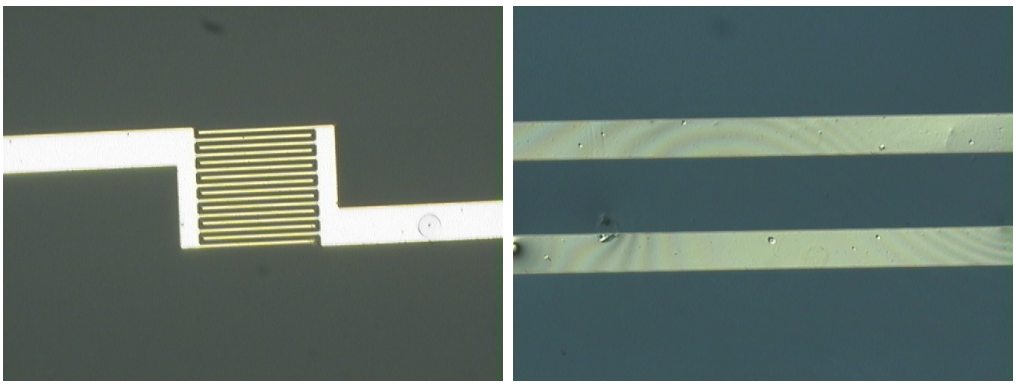

Figure 3.12: On the left Q14 Set 1 Electrode 2 before application of curing agent. On the right an example of the electrode lines after application of curing agent. The fringes indicate the presence of a thin transparent film on top of the gold electrodes.

To test if curing agent would in fact create a thick film on the surface of the die we first ran a thermal deposition with a small amount of curing agent on a hot plate and a die above it. Not surprisingly, a thick layer of curing agent deposited on the die; Fig. 3.12 shows before and after microscope images. Unfortunately, it was difficult to see the clear film on the small surfaces of the interdigitated electrodes but fringes on the larger electrode lines

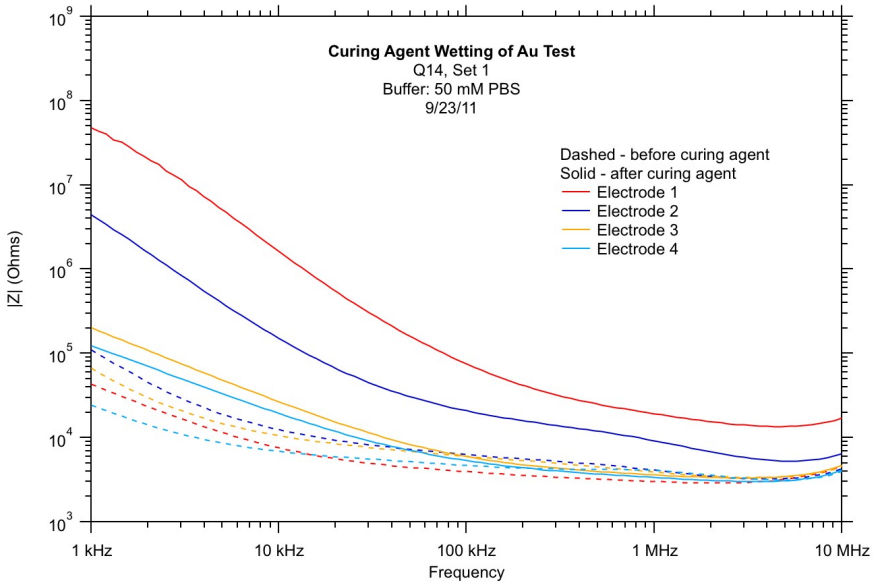

(a) Impedance measurements of Q14 Set 1 before and after application of curing agent.

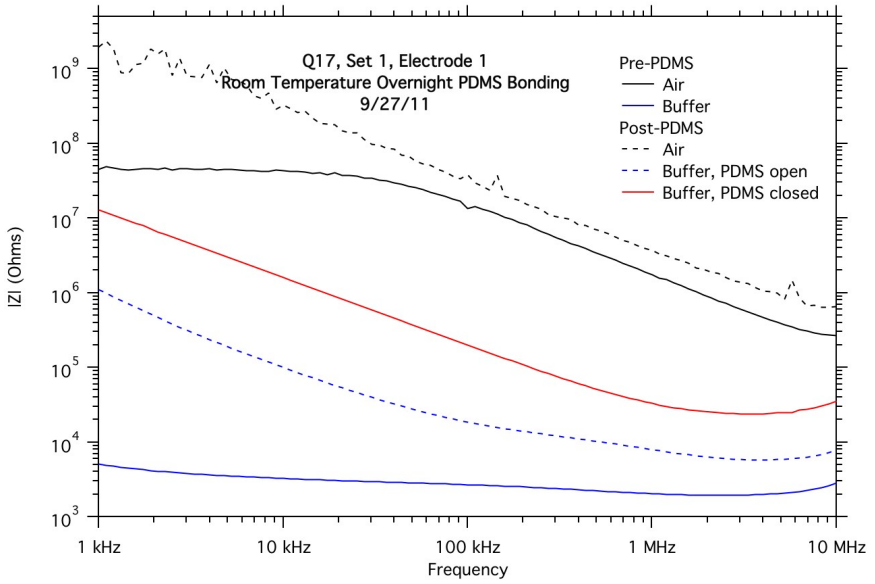

(b) Impedance measurements of Q17 Set 1 Electrode 1 before and after application of curing agent and PDMS.

Figure 3.13: Changes in impedance with application of curing agent with and without PDMS.

made it more apparent. We then looked into how curing agent affected the impedance scans by taking impedance measurements with and without curing agent on the device (see Fig. 3.13a). Buffer solution was placed on the electrode sets and scans were taken (dashed lines) after which the sample was cleaned and a couple of droplets of curing agent were placed on the device away from Set 1. The die was then placed on the hot plate at 90°C for 5 minutes. Scans with an equivalent amount of buffer solution were again taken (solid lines). It appeared placement of curing agent could significantly contaminate the electrodes.

After determining that the use of curing agent caused contamination of the electrode surfaces, we fabricated a device and took impedance measurements before and after application of curing agent. With this device a heat cure was not performed, but instead the device sat overnight at room temperature to complete the bonding step to decrease contamination from the curing agent. The device still showed significant fouling after PDMS bonding as shown by much increased double layer capacitance in buffer after PDMS application (see Fig. 3.13b). The double layer capacitance is caused by effects on the electrode surfaces and appears at higher frequencies which we see in Fig. 3.13b comparing buffer impedances before and after curing agent (solid and dashed blue traces).

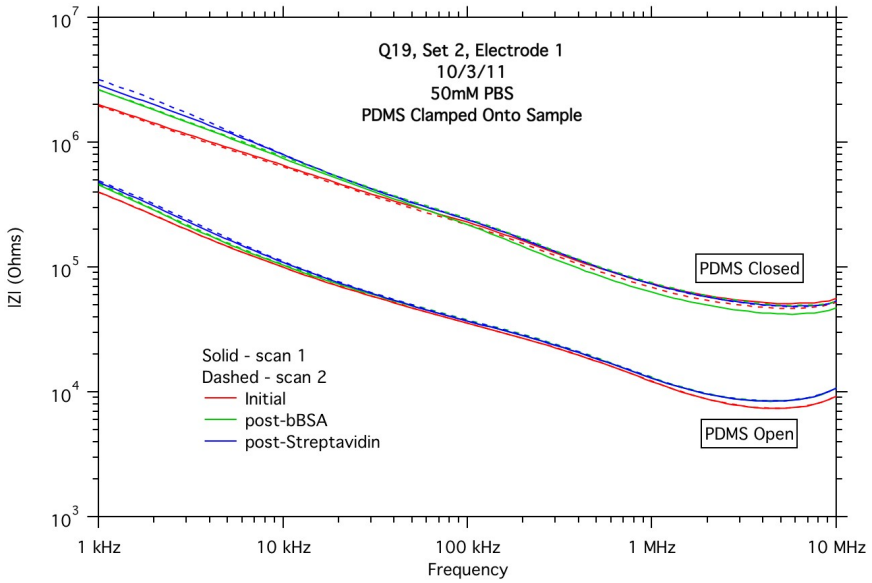

Figure 3.14: Q19's sensing run with BSA and streptavidin.

Curing agent appeared to be the source of the problems. Therefore we determined to attach PDMS without using curing agent to bond the device. For this purpose we built an acrylic clamp. Using only the clamp for PDMS to quartz attachment we tested several other dies. However, the results of these experiments didn't look promising either (see Fig. 3.14). Neither the introduction of BSA or streptavidin changed the impedance through the sensor much, as shown by the closely spaced results in both open and closed cases before and after introduction of the biomolecules.

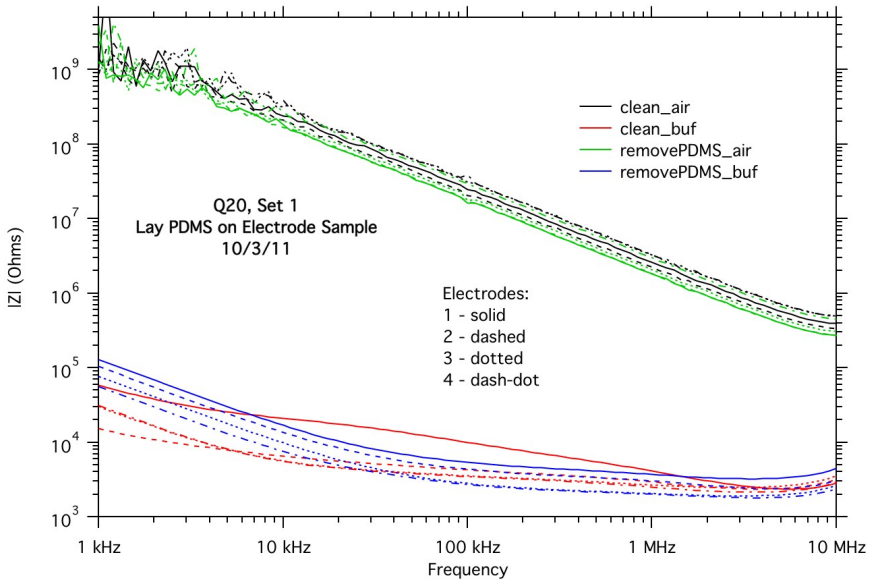

Figure 3.15: Impedance measurements before (blue and red traces) and after (green and black traces) clamping PDMS onto a quartz sample.

In order to determine if the PDMS was out-gassing oligomers we scanned the impedance before clamping PDMS onto the die, clamped a piece of PDMS on for an hour, then removed the PDMS, and scanned again (see Fig. 3.15). Even without curing agent or a lengthy exposure time, PDMS appeared to be out-gassing onto the surface of the die and affecting the impedance of the electrodes. This out-gassing happens because PDMS is mixed with curing agent and the polymerization process leaves oligomers which can leach out. However, the effect on the electrodes didn't seem to be great, and in the buffer scans (red and blue traces in Fig. 3.15) it even appeared to decrease the variance between electrode impedances.

3.2 Microchannel impedance sensors

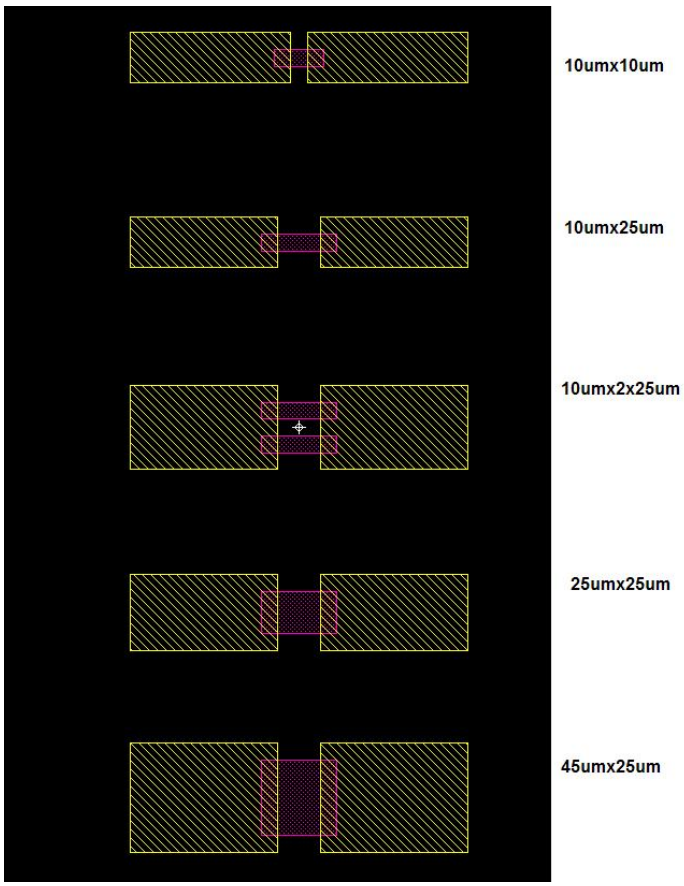

Figure 3.16: Mask for microchannel impedance sensor design, red areas are the etched microchannels.

We had developed a better understanding of curing agent and the consequences of its use but this understanding still didn't explain the results. The curing agent appeared coat the electrodes but even when we took steps to minimize the coating we had inconsistent results with BSA and streptavidin. We designed a simpler sensor for ease of analysis and troubleshooting. This was accomplished by removing the interdigitated electrode fingers and etching a channel (red area) between the electrodes (see Fig. 3.16). In conjunction with the PDMS valves this would concentrate the ionic conduction path to the single etched trench or microchannel connecting the electrodes. To test different microchannel widths and electrode spacings, five designs were fabricated (see Fig. 3.16). One set of five designs was

arranged under one PDMS valve while another set without etched trenches was placed as a reference under the adjacent PDMS valve. The PDMS design remained unchanged from the interdigitated electrode sensors.

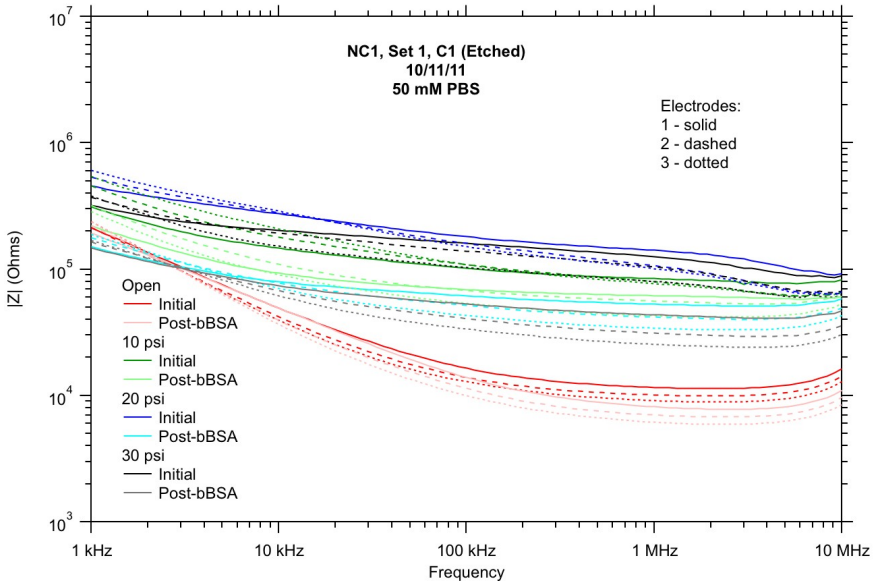

(a) Impedance sensing results from NC1 Set 1.

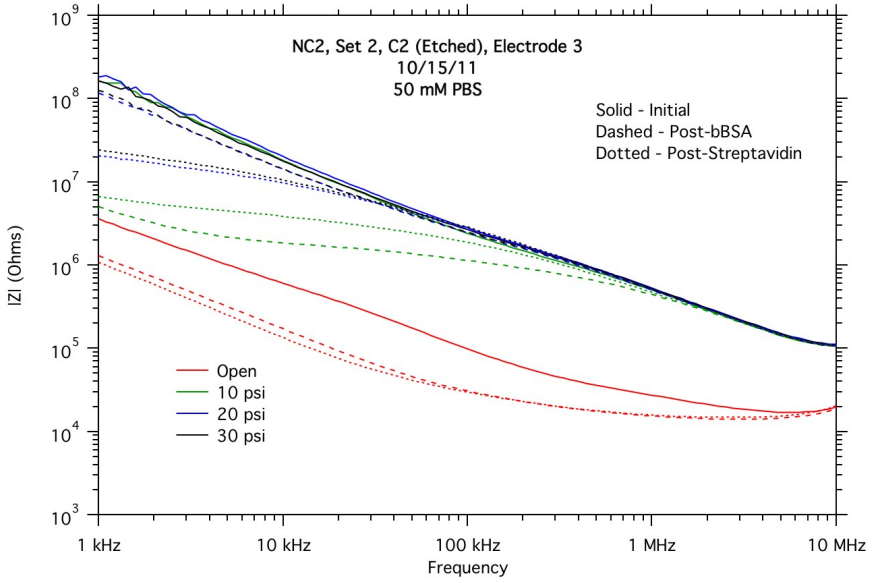

(b) Impedance sensing results from NC2 Set 2.

Figure 3.17: Impedance sensing results from microchannel sensing runs.

We ran tests on the microchannel sensors similar to those run on the other impedance sensors. After protein introduction to the sensors the impedance between the electrodes decreased in both runs (see Fig. 3.17a and Fig. 3.17b). The data from the second run in particular (see Fig. 3.17b) indicated the PDMS was sealing off the microchannels themselves as the black 30PSI traces look to follow a parasitic capacitance curve. This was likely caused by the PDMS conforming over the edges of the electrodes or conforming into the microchannel. This was a troubling development because it would make the sensor more sensitive to changes in the PDMS conformation, actuation pressure, and small differences in fabrication than the presence of biomolecules.

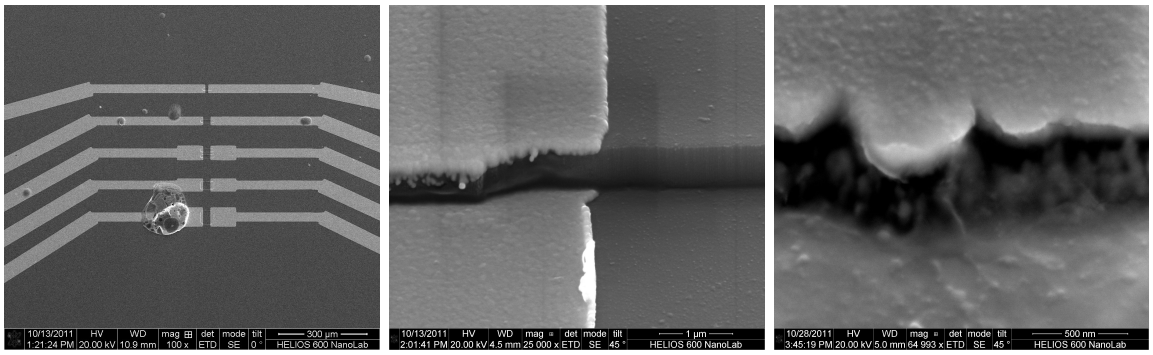

Figure 3.18: SEM images of NC1 and NC2 microchannel impedance sensors.

To gain a greater insight into the microchannel sensors and how the PDMS might be conforming into the microchannels we took images of the sensors in a scanning electron microscope (see Fig. 3.18). The images showed the gold electrodes didn't connect at the microchannel sidewalls. This confirmed that it was possible for the PDMS to conform over the electrode surfaces cutting off the electrodes from the microchannel and rendering impedance measurements meaningless. Thicker electrodes were fabricated to coat the sidewalls but they exhibited similar problems. Unfortunately much thicker films would likely delaminate from the substrate despite the chrome transition layer beneath, especially with the added mechanical stress of the PDMS valve actuations.

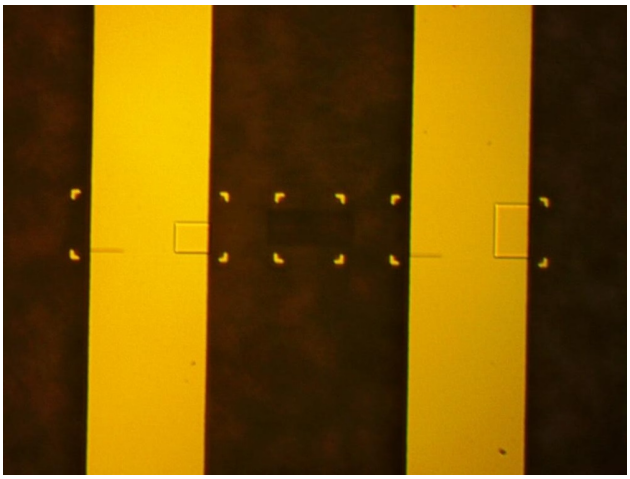

(a) Fabricated nanochannel array.

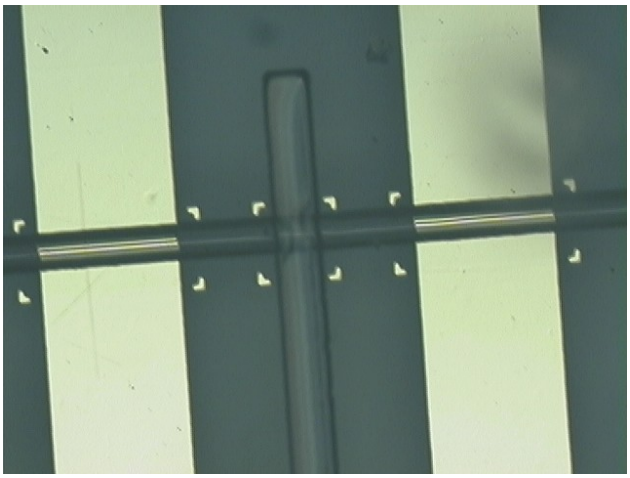

(b) A fabricated PDMS valve placed over an array of nanochannels.

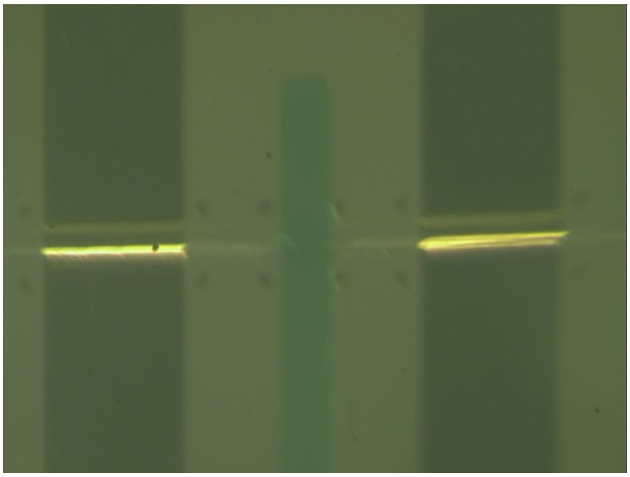

(c) PDMS valve actuated on an array of nanochannels.

Figure 3.19: Microscope images of a nanochannel array and PDMS valves.

3.3 Nanochannel impedance sensors: design A

The previous design had valves which could conform around the electrodes making them inadequate for biomolecule detection. The trenches were also wide enough that the PDMS valves could partially collapse into the opening. This partial collapse could introduce more variability into sensing results as minute differences in actuation pressure, fluid pressure, or valve seating could affect the resulting channel height. We developed a sensor where the PDMS valve would close over a section of nano-trenches. These nano-trenches have widths around a 100nms, much closer to the size of the proteins being detected, which should provide much greater impedance changes after protein attachment. Fig. 3.19a shows the location of a fabricated array of nano-trenches. The alignment marks are for working with the Helios Nanolab 600 (FIB), in the center of the marks is a darker section of lines, this is the nano-trench array. The newly designed PDMS valves didn't close over the length of the nano-trenches but left openings on both sides for ionic conduction through the newly formed nanochannels. Fig. 3.19b shows the placement of the PDMS valve well within the alignment marks while the nanochannel array extends beyond the marks. Fig. 3.19c shows an actuated PDMS valve. The narrow trenches prevent the PDMS valves from varying significantly in how deeply they conform into the trench openings.

After deciding to work on nanochannel sensors we designed a sensor on an one inch by one inch quartz die with the hope of sensing a panel of twelve biomarkers. The promise was not fulfilled in this iteration of the device. This particular device required some modification to be able to detect any biomolecules at all due to a design flaw. It also demonstrated how easily the nanochannel arrays could be multiplexed. As sometimes happens we were focused almost entirely on the necessity of fabricating a new working PDMS valve that we neglected to see the big picture. The flaw in this sensor is that while one side of the device had a carefully fabricated column of nano-trenches and valves above them (right side of Fig. 3.20a the fluidic channel is green while the valves are purple), on the other side of the valve was another microchannel overlapping the same electrodes (the green line on the left in Fig. 3.20a) and guaranteed to have an impedance much lower than that of the nanochannels. This lower impedance in parallel with the much higher nanochannel array impedance made detecting changes in the nanochannel array practically impossible. This design flaw wasn't

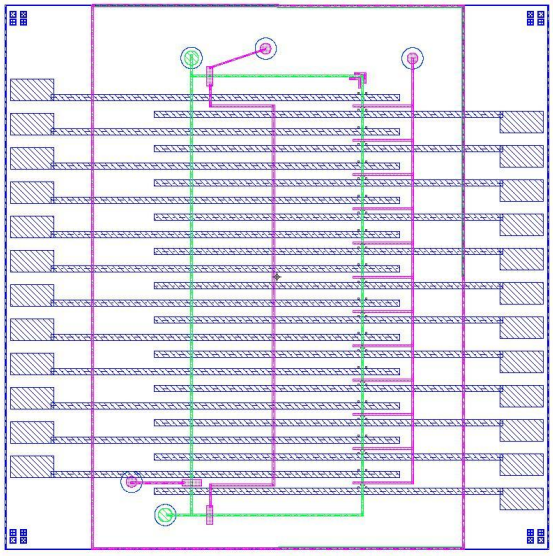

(a) First generation nanochannel sensor and PDMS schematic.

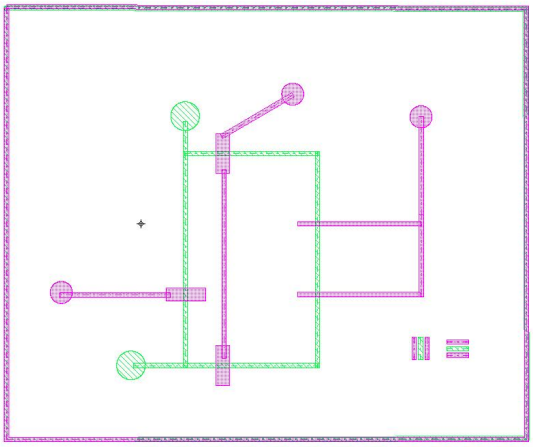

(b) Second generation PDMS schematic.

Figure 3.20: Schematic design of initial nanochannel sensors.

noticed immediately after testing started on the die because of another difficulty with the design. The fluid channels were much smaller than we had used before and could only handle much slower flow rate than previous designs. These flow rates required more time per experiment and so we abandoned the larger PDMS piece for a smaller, more manageable design (see Fig. 3.20b). Unfortunately this PDMS design also suffered from the same parallel fluid channel flaw as the larger PDMS piece making meaningful sensing results difficult to obtain.

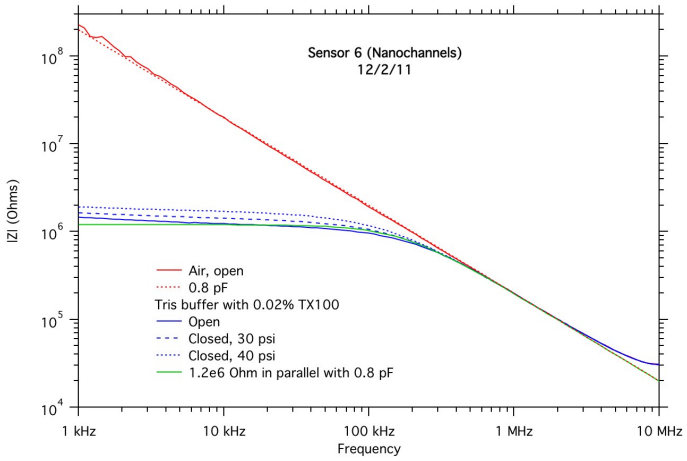

(a) Results of a nanochannel experiment with NC3 with Sensor 6.

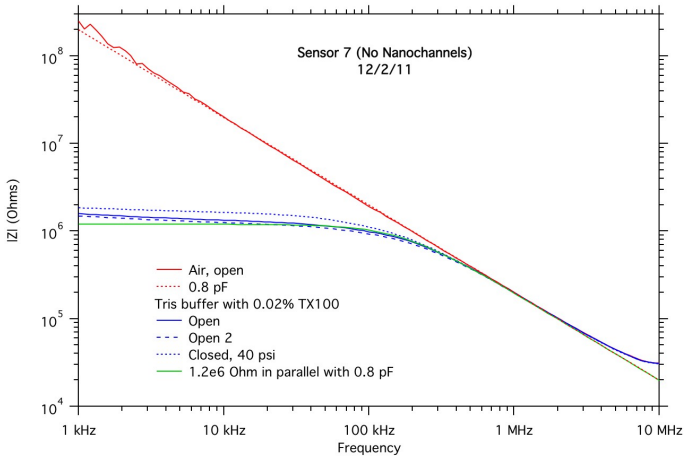

(b) Results of a nanochannel experiment with NC3 with Sensor 7.

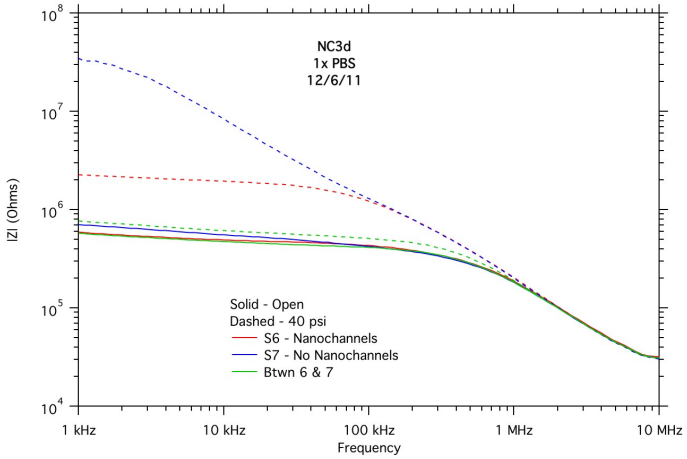

(c) Results of nanochannel buffer experiment with NC3d.

Figure 3.21: Results of the first sets of nanochannel experiments and a later design.

With the PDMS design, the results we got from the first nanochannel sensor were exactly what we should have expected to get. The traces in air follow the parasitic capacitance curve and with fluid in the channels the impedance is considerably smaller (see Fig. 3.21a and Fig. 3.21b). After the valves are actuated the impedance goes up, but only slightly. This behavior is consistent with the lower impedance caused by the bypass channel in parallel with the increased impedance on the sensing channel after the valves have been actuated. Shortly after getting these results the flaw in the design was recognized.

This smaller PDMS could still be used to run a few tests, it needed only to be rotated 180° so the bypass channel was on the right side of the quartz die and didn't electrically connect adjacent electrode lines. The last graph shows the results from one of those runs (see Fig. 3.21c). This is promising as the buffer trace from S6 with nanochannels (dashed red) starts to look resistive at 100kHz, consistent with ionic conduction through the nanochannels. Even more promising is that S7 without nanochannels (dashed blue) followed the parasitic capacitance curve closely, suggesting the PDMS valve electrically isolated adjacent electrodes. This isolation between non-nanochannel electrodes allowed us to trust the nanochannel impedance we obtained.

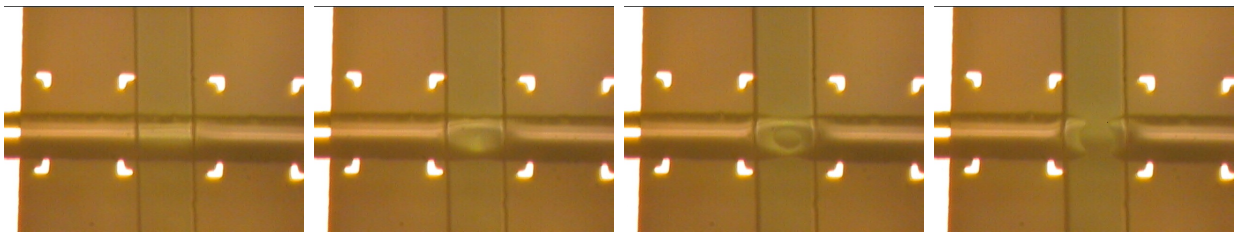

Figure 3.22: Images of a PDMS valve at different actuation pressures 10PSI, 20PSI, 30PSI, and 40PSI.

With this design we continued exploring how PDMS valves behaved in their dynamic nanochannel function. Fig. 3.22 shows a series of the valves closing at different pressures. To obtain reliable sensing results we desired PDMS valves which would close across the nanochannel array consistently. As shown in Fig. 3.22 the valves didn't close until after 30PSI, a much higher pressure than we desired. Our testing equipment wasn't built to

handle pressures around 40PSI. Working at that high of a pressure wasn't desirable for eventual use as a sensing platform either as it increases costs and complexity.

3.4 Nanochannel impedance sensors: H-Valve PDMS design

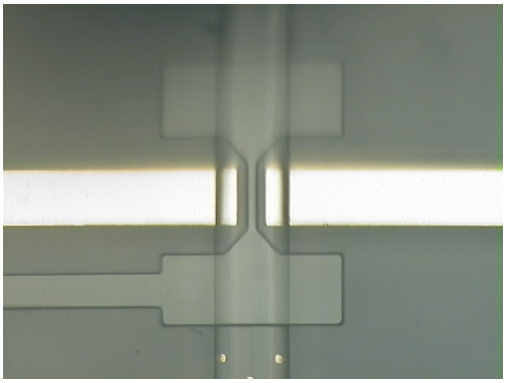

(a) Microscope image of fabricated H-bar valve.

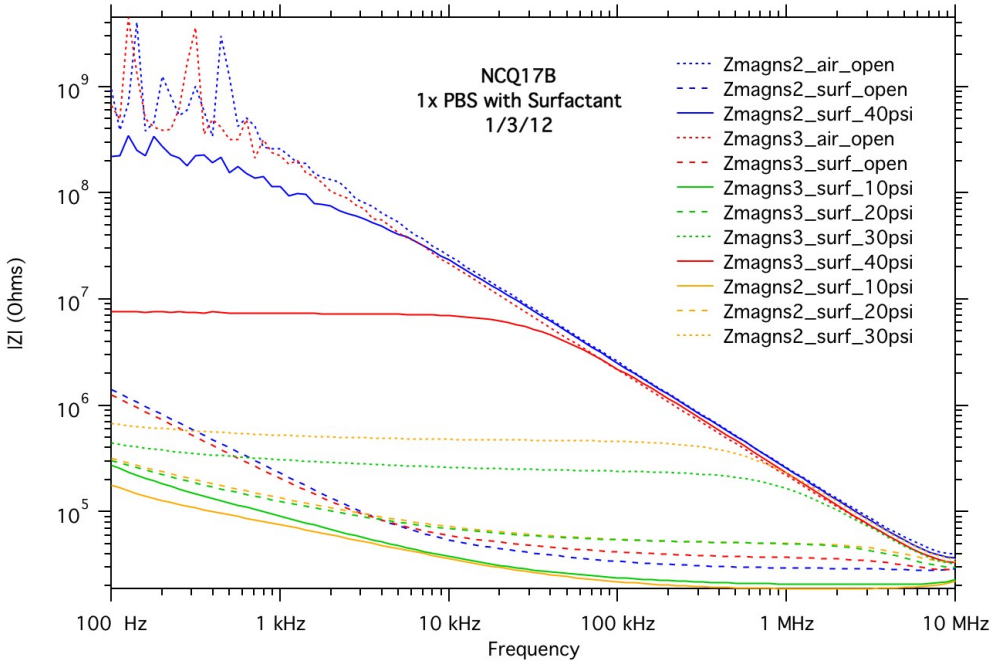

(b) Results from H-Valve nanochannel characterization experiment.

Figure 3.23: A fabricated H-valve and results from a characterization experiment.

Though the initial nanochannel sensors were promising, we wanted PDMS valves which would close more reliably and at a lower actuation pressure. These valves needed to be thin enough to fit over the milled nanochannel trenches and still close reliably. In the earlier PDMS designs all valves were designed to have the same width as the channels they were closing. To allow a significant amount of flow through the channel we wanted fluid channels much wider than 100μm. With a valve width greater than 100μm it would require nanochannels with lengths longer than 100μm and an array of hundreds of them to keep the overall impedance of the nanochannels under the parasitic capacitance curve. Using the FIB is more expensive and time consuming than other fabrication steps necessitating a design with shorter nanochannel lengths. In addition to the practical cost and time considerations, we believed from Fig. 3.22 that the parts of the microchannel channel hardest to seal were at the edges (as seen in the 30PSI image). At the edges of the channels the PDMS membrane is the thickest making them logically the hardest portion of the channel substrate for the PDMS valve to collapse. Therefore we fabricated a "H-valve" which closed parallel to the channel with a narrow bar (see Fig. 3.23a) and much thicker regions on the sides. The thickness of the narrow bar section of the H-valve varied from $25-75\mu$m as we characterized the new valve.

This valve closed, but also didn't seal completely until 40PSI. Fig. 3.23b shows a characterization run of the H-Valve PDMS design. As with the previous nanochannel design at 40PSI in buffer the sensor with nanochannels goes resistive (solid red trace) under about 70kHz and without nanochannels (solid blue trace) looks capacitive. Unfortunately there is a large gap between the 40PSI traces and the 30PSI traces (dotted yellow and dotted green) suggesting they were only just closing over the nano-trenches. We reasoned it was because the H-valve trapped fluid in the two pockets at the top and bottom of the "H". The fluid in these pockets had a difficult time flowing under the wide valve regions when the valve was actuated. After some consideration we truncated the top right and the bottom left portions of the H-valve creating what we called the "S-valve" which will be discussed in the following chapter.

Chapter 4

A Dynamic Nanochannel Array Sensor

In this chapter I report fabrication of a PDMS (polydimethylsiloxane) and quartz dynamic nanochannel sensor and demonstrate the viability of the sensor with nonspecifically bound BSA. The observed response is consistent with multilayer BSA coverage on the channel walls.

Nanochannel sensors have much promise in biomarker testing; however, transporting a significant number of biomakers at low concentrations to the sensor surfaces is challenging. To help increase the volumetric flow rate and introduce biomolecules at a faster rate we introduce the concept of dynamic nanochannels. These consist of nano-trenches where a section of the open side can be dynamically sealed off to form nanochannels (see Fig.4.1). To close the top opening of the nano-trenches a valve with a narrow bar 35μm wide is centered on the nanochannels. When the valve is actuated an array of nanochannels is formed. To ensure the only ionic path between the electrodes is through the nanochannels the valve also seals off a portion of both ends of the microchannel. The microchannel allows for analyte to be introduced to the top of the nano-trenches at flow rates higher than those achievable in traditional nanochannel sensors. Unlike traditional nanochannels, all of the analyte is not flowed through the nanochannels themselves, meaning the fluid should be recirculated for optimal sample use. Thus dynamic nanochannels incorporate the advantages of the small dimensions of traditional nanochannel impedance sensors for measurement purposes while utilizing the high flow rates of microfluidic devices. As the nanochannels are located at the bottom of the flow channels they don't suffer from the strong shear forces the molecules in traditional nanochannels can be exposed to.

The dynamic nanochannels are made with nano-trenches fabricated with a FIB in a quartz substrate and a PDMS (Sylgard 184 kit; Dow Corning Corp.) valve situated

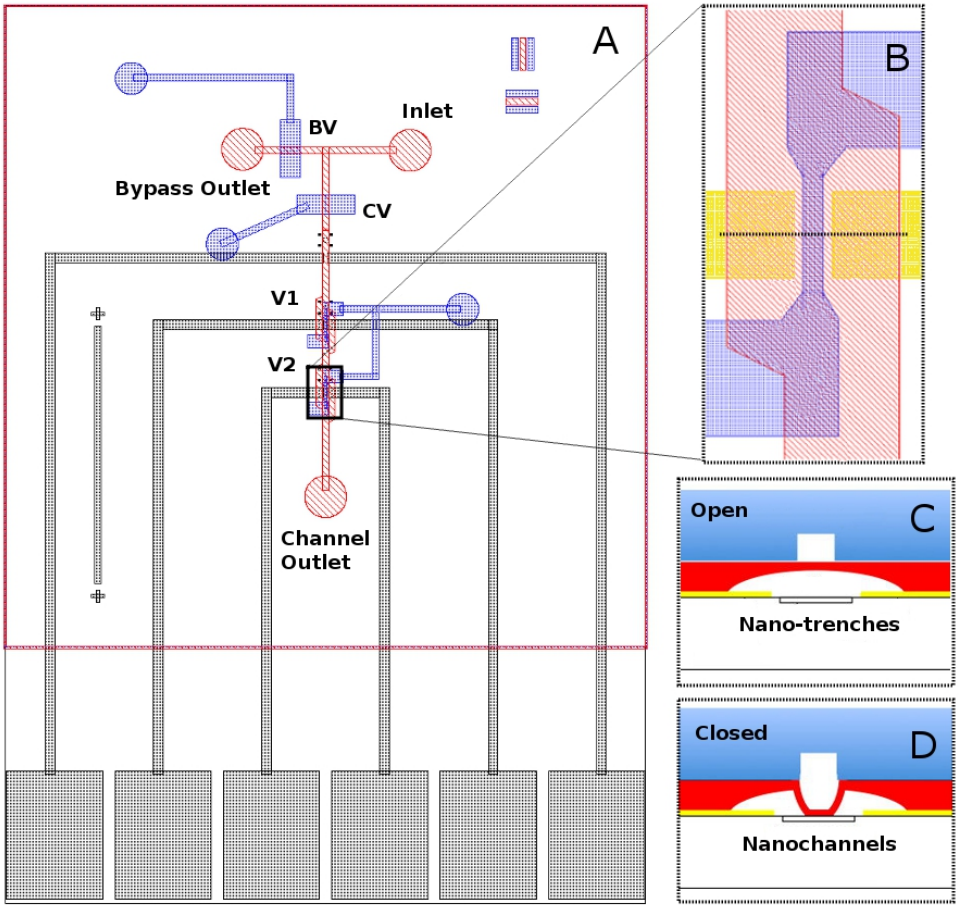

Figure 4.1: A: Schematic diagram of device with two sensor regions, V1 and V2, both of which are under PDMS valves. V2 has nanochannels etched into the quartz while V1 does not. B: Top view of V2. C&D: Cross section views along dotted line in B for open and closed conditions of the valve.

above them (see Fig. 4.1C). When the valve is actuated a section of the nano-trenches is sealed forming nanochannels (see Fig.4.1D). With the valve open a microfluidic channel is exposed allowing rapid transport of analyte to the surfaces of the nano-trenches (see Fig.4.1B&C). The valve is composed of two PDMS layers: the fluid layer (red in Fig.4.1) and the control layer (blue in Fig.4.1). The microchannels are formed in the fluid layer. Above the microchannels the control layer has control channels filled with DI water. To actuate the valve these channels are pressurized deforming the fluid layer membrane beneath and sealing a section of the fluid channel (see Fig.4.1D).

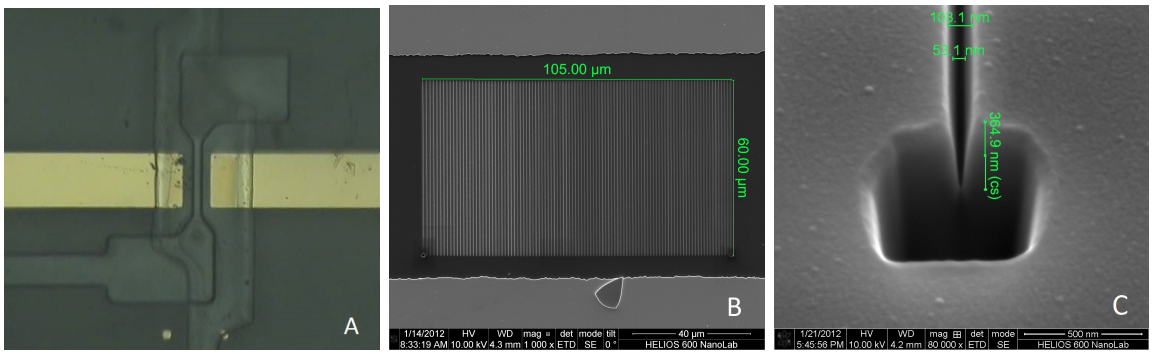

Figure 4.2: A: Microscope image of fabricated sensor region. B: Nano-trench array after FIB milling. C: Close up of a single nano-trench.

To fabricate the sensor, first a 100mm quartz wafer (University Wafer) is dehydration baked at 150°C for 10min. Surpass 4000 followed by a layer of AZ701 are spin coated onto the wafer, each at 4000rpm. The wafer is then soft baked at 90°C for one minute. Next, a 10 second exposure is done with the mask containing the electrodes and the photoresist is developed for 20 seconds in MIF300. We rinse with DI water followed by a thermal deposition of 15nm of chrome and 150nm of gold onto the wafer. A lift-off is performed in an ultrasonic bath for 20 minutes with Microposit 1165. After the lift-off the wafer is again rinsed with DI water.

Nano-trenches are created by milling with a Focused Ion Beam (FIB). To decrease charging during milling, a 32 nm layer of aluminum is first evaporated onto the wafer surface using an electron-beam evaporator. A total of 141 lines are then milled into the quartz surface with the FIB (see Fig.4.2B&C). The wafer is then placed in nanostrip for five seconds. After being exposed to the nanostrip the wafer is rinsed in DI water. The aluminum layer is completely removed by submerging the wafer in aluminum etchant for 15 minutes. Finally, the wafer is rinsed with DI water, acetone and IPA (isopropyl alcohol) followed by a blow dry with nitrogen gas.

The top or control layer of PDMS is fabricated with a 4:1 ratio of PDMS to curing agent. The control channel mold is made with SU8-2025 and after fabrication had a thickness of 24μm.

The PDMS for the fluidic layer is a 30:1 mixture of PDMS to curing agent. This ratio made the PDMS exceptionally flexible to seal off the nanochannels when the valves

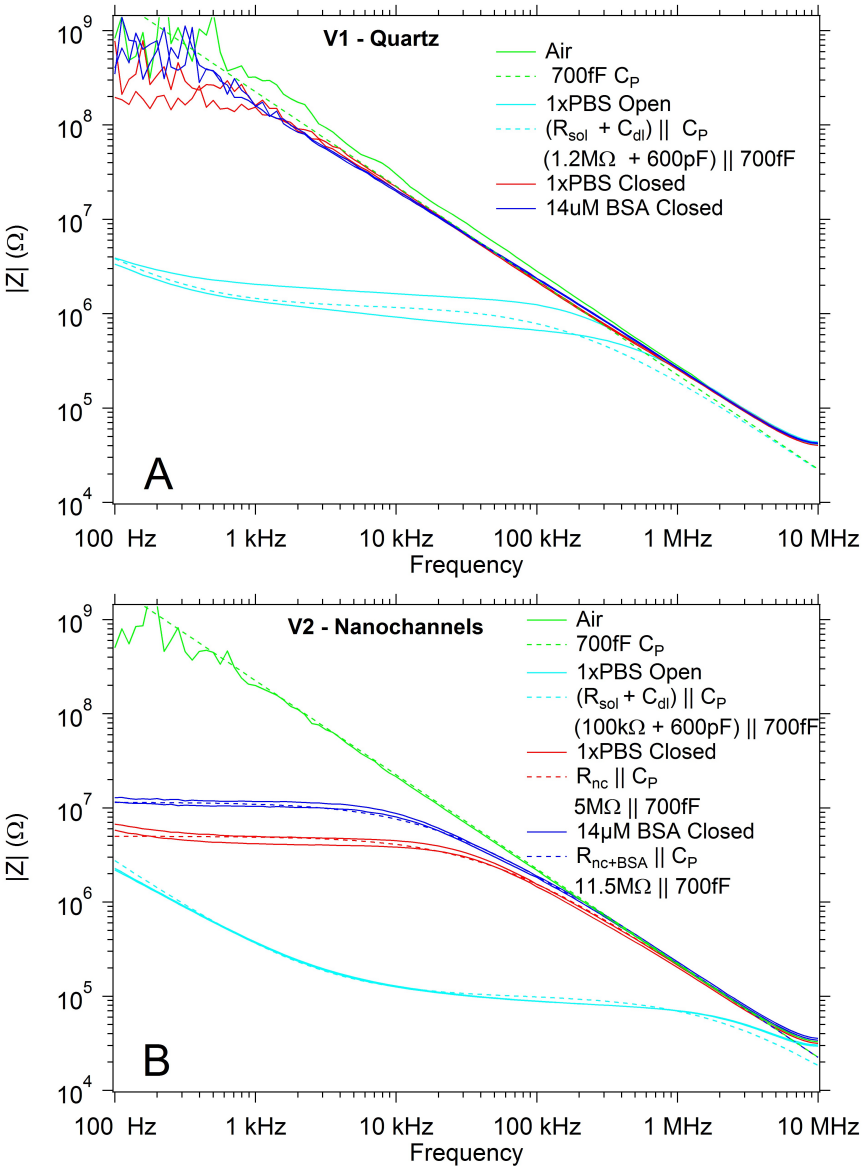

Figure 4.3: Impedance measurements for V1, V2 and fitted data. Solid lines are the measured impedances, dashed lines are circuit equivalents. Green traces are the scans in air before introducing fluid. The light blue curves are the fluid impedances with open valves. blue and red traces are with the valves actuated, blue after BSA has been introduced and red before.

were actuated. To make the mold for the fluidic layer, a four inch silicon wafer is baked in the dehydration oven for ten minutes. HMDS is spun onto the surface at 4000 rpm for one minute followed by a one minute bake at 90°C. SPR220-7.0 photoresist is then spun at 430 rpm for five seconds then 2000 rpm and 4000 rpm for 60 seconds each. A proximity softbake is then performed at 115°C for 120 seconds. The wafer is then exposed to the fluidic mask for 35 seconds at six mW/cm^2. After exposure the wafer is developed in MF-24A for five minutes then rinsed in DI water and dried with nitrogen gas. The wafer is then baked at 110°C for one minute to reflow the photoresist. Post reflow, the channel mold has a semicircular profile with a height of 8μm and a width of 300μm. After mixing, the PDMS solution is degassed for 50 minutes. The wafer is then silanized ((tridecafluoro-1,1,2,2-tetrahydrooctyl)-1-trichlorosilane, UCT Specialties (Bristol, PA)) on a hotplate at 70°C for 10 minutes to decrease PDMS-to-mold binding. After which the PDMS is spun onto the wafer at 500 rpm for five seconds followed by 4500 rpm for 60 seconds. An oven bake at 80°C for 45 minutes is then performed.

After stamping with curing agent, the PDMS piece is bonded to the quartz piece and cured on a hot plate at 70°C for 30 minutes [29]. The sensor is then clamped in an acrylic holder with holes drilled in the top piece for the fluid and control lines. The clamp is necessary to help the sensor valves to close fully in that there is no conduction path between electrodes except through the nano-trenches in V2.

Impedance measurements are performed with an Agilent 4294A Impedance Analyzer. 4.3 shows the results of the impedance measurements taken (solid lines), as well as traces representing an equivalent circuit (dashed lines). After an initial air scan (the trace labeled "Air" in Fig. 4.3) the control channels are filled with DI water. Then a 1xPBS solution is introduced to the sensors. Fluid is introduced via the Inlet (see Fig. 4.1). When changing fluid a bubble separates the different sensing fluids. The bypass channel provides a path for the bubble to flow through the device without interacting with the nano-trenches. A Harvard Apparatus Pump (PHD 2000) pushes fluid through tubes into the device inlet at a pressure of 25PSI. After the flow is stopped the clamp is tightened until V1 closes completely when actuated as shown by the impedance measurement approaching $10^9\Omega$ at 100kHz. The clamp remains at the same pressure for the remainder of the experiment. A series of scans

are then conducted with the valves alternately open and closed with the valves pressurized to 40PSI (1xPBS Open and 1xPBS Closed in Fig.4.3). A 1xPBS solution with 14μM BSA is then flowed through the microchannel above the nano-trenches for 15 minutes. After BSA exposure the channels are flushed with 1xPBS and a series of impedance scans are taken (14μM BSA in Fig.4.3).

In the fabrication and testing process we discovered that it was a challenge to have a PDMS valve seal completely to ionic conduction. Some iterations of the valves appeared shut to flow but still had ionic conduction. Wide PDMS valves were easier to seal to ionic flow. However we wanted the overall impedance of the nanochannels to be less than $10M\Omega$. We could decrease impedance by adding more nanochannels or decreasing the width of the valve. We settled on a 35μm valve width with 141 nanochannels, thereby allowing the nanochannel impedance to be in the range we desired and keeping overall processing time down. To enable this device to close reliably to ionic flow with a 35μm valve width we placed the device in an acrylic clamp and actuated the valves at a pressure of 40PSI. The top side of the clamp provided pressure and a solid surface to allow the valve to seal electrically. Due to the pressure from the clamp and variations in the control layer thickness the microfluidic channel partially collapsed in different areas of the die. These collapses led to different open impedance measurements between V1 and V2.

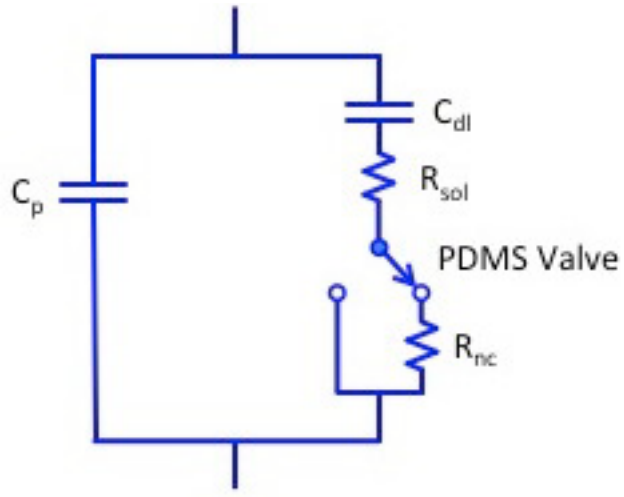

Figure 4.4: Equivalent electrical schematic of the dynamic nanochannel sensor.

An equivalent circuit model for the device is shown in Fig.4.4. There is a parasitic capacitance (C_p) associated with any electrical component. This capacitance sits in parallel with the other circuit elements and sets an upper bound on the measurable impedance. C_p is modeled by a 700fF capacitor (see Fig.4.3). There is also a double layer capacitance (C_{dl}) representing the electrical double layer which forms on the surface of the electrodes. The impedance of the double layer capacitance can be seen in the lower frequencies when the valves are open (see Fig.4.3). C_{dl} corresponds to a 600pF capacitor. The 1xPBS solution has a conductivity of 1.6 x10^{-2} S/cm [31]. When the valve is open this leads to a certain impedance R_{sol} representing the impedance of the solution in the microchannel. When the valve is closed (represented by the PDMS Valve switch in Fig.4.4) R_{sol} is then in series with either an open circuit for V1 or the nanochannel resistance R_{nc} in V2. R_{nc} is much greater than R_{sol} so changes in the ionic path through the nanochannels dominate the overall impedance.

V1 is fabricated as a reference to ensure the PDMS valves seal completely to ionic flow. When the valve is actuated the sensor impedance as a function of frequency looks capacitive. This capacitive curve confirms the valve is an effective insulator between the electrodes. With the valve open the impedance is higher than predicted. The resistance between the electrodes with the valve open and a fluid channel with a height of 8μm should have approximately 26kΩ of impedance, but we see a considerably higher impedance of 100kΩ. This is consistent with a channel height of 0.2μm, indicating that the flow channel is largely collapsed in this region due to the pressure.

In the open case V2 has around 4x more impedance than calculated. The impedance is consistent with a channel height of about 2μm. When closed, V2 behaves as expected. Calculating the impedance of 141 nanochannels with height 380nm, width 65nm and length of 35μm gives 7MΩ, which is consistent with the 5MΩ measured result. The difference is to be expected as it would be surprising for the nanochannels to seal fully across the 35μm width of the valve. A 5MΩ impedance corresponds to the valve sealing off 25μm of the nanochannels (see Fig.4.1D). Once BSA has been introduced to the sensors the impedance of the nanochannel array goes up to 11.5MΩ.

The change in the ionic conduction path of a triangular nanochannel upon adsorption of protein onto the walls is given by $\frac{w_0^2}{(w_0-2t)^2} - 1$ where w_0 is the width of the nanochannel opening and t is the thickness of the adsorbed protein layer. Using the impedance change at 2kHz and assuming the protein layers are evenly distributed along the length of the nanochannel walls with a width of 103nm and a depth of 380nm there is a layer of protein 18nm thick on the sensor walls (see Fig.4.5). BSA is has been reported to be between 4nm and 8nm in diameter suggesting a multilayer covering of the protein on the channel walls [28]. A 4nm monolayer of BSA covering the nanochannel walls should yield a 17% impedance change.

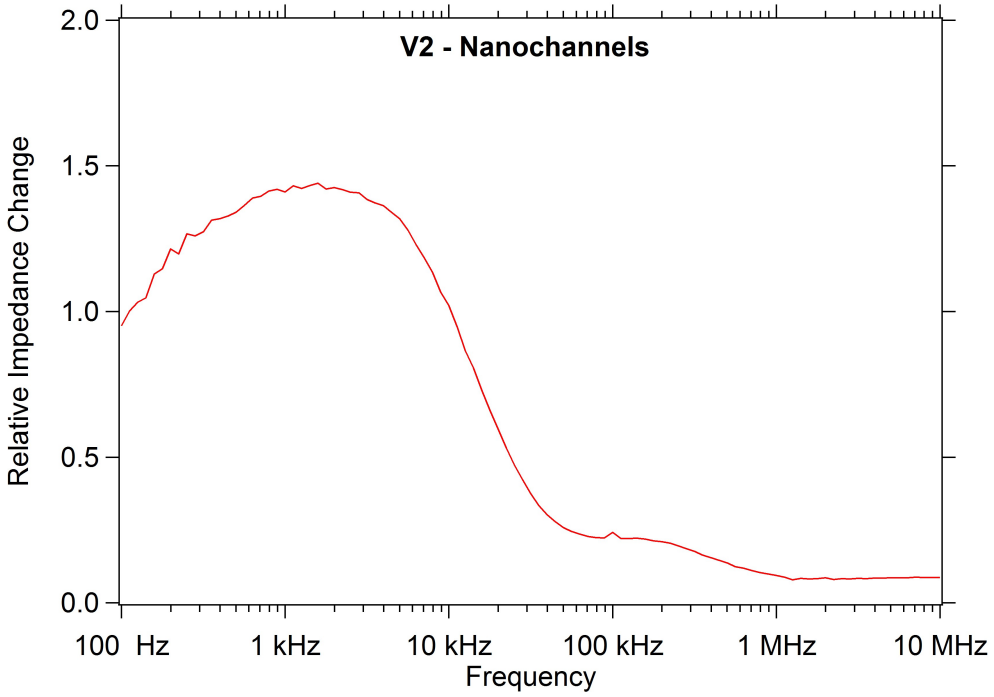

Figure 4.5: Relative impedance change ($\frac{|Z_f|-|Z_i|}{|Z_i|}$) from before and after BSA introduction as a function of frequency.

The large relative change in nanochannel width equates to a large change in the effective impedance of the device. At 2kHz the measured impedance change was 140%. Our tests are run with a 1xPBS solution so surface effects on the electrodes or the nanochannel surfaces themselves would not play an important role in the overall conductance [22].

We introduced analyte to the sensors in only 15 minutes. The Hagen-Poiseuille law for a rectangular pipe having a pressure drop of 25PSI across the length of the microchannel with an average height of 2μm (calculated open height of V2) and width of 300μm the fluid gives a volumetric flow rate of 5.75nL/s or an average velocity of 9.6mm/s. This high flow velocity increased the rate of biomolecule attachment to nanochannel walls.

There are several paths towards improving the detection limits of dynamic nanochannels. The size of the bound biomolecule layers compared to the width of the nanochannels determines the relative impedance change. By decreasing the width of the nanochannels the impedance change can be increased. Moreover, after the biomolecules have adsorbed to the nanochannel walls a large labeling molecule specific to the biomolecule could be flowed and attach to the analyte. This would increase the effective size of the bound layer on the surfaces, also greatly increasing the sensitivity. Another promising way to improve the dynamic nanochannel sensor would be to replace PDMS with another microfluidic material or method which would more readily close to ionic flow.

In conclusion, we have built and tested a dynamic nanochannel sensor. This sensor works by using valves and fluidics that are often already included on nanochannel devices. The dynamic nanochannel sensor offers the measurement abilities of traditional nanochannel sensors but also incorporates the increased flow speeds available with microfluidic devices. These increased flow rates should allow the dynamic nanochannel sensor to detect concentrations of analyte which were previously impractical to detect using nanochannel impedance sensing.

Chapter 5

Biomolecular Flux and Detection Limits

The goal of this chapter is to determine the detection limit for the dynamic nanochannel channel sensor. The sensor's detection method requires biomarkers to be immobilized to the nanochannel walls by receptor molecules already bound to the walls. The bound biomarkers will reduce the available volume for ionic conduction in the nanochannel. If there are sufficient numbers of biomarkers immobilized this increased impedance can be measured and the presence of the biomarker determined. As has been noted the biomarker concentration required for medical purposes is often in the picomolar range. With these concentrations, attaching a significant number of biomarkers to the sensor walls becomes a challenge. Therefore, quantifying the number of biomarkers that attach to the sensor wall for a given concentration is crucial in determining detection limits for the dynamic nanochannel sensor. In addition, the variability when actuating the PDMS valve between successive runs will play a role in determining the minimum detectable impedance change.

When working with picomolar concentrations, the rate of molecules attaching to the sensor surfaces often becomes the limiting factor in sensing applications. In the case of typical static nanochannel sensors, unless the fluid has a velocity greater than several millimeters per second, all of the analyte within the sample volume will encounter the sensor walls [23]. With these flow rates all of the biomarkers have the ability to bind making static nanochannel sensors very efficient with sample volume. The HagenPoiseuille equation relates fluid channel dimensions to pressure and fluid flow [32]. As electricity was historically considered a fluid these terms relate easily to circuit terminology with pressure drop corresponding to voltage, volumetric flow rate to current and channel dimensions in conjunction with the viscosity of the fluid providing the analogue to resistance. Nanochannels correspond to very high impedance resistors. Ohm's law tells us $V = IR$ or $I = \frac{V}{R}$; the flow resistance of static

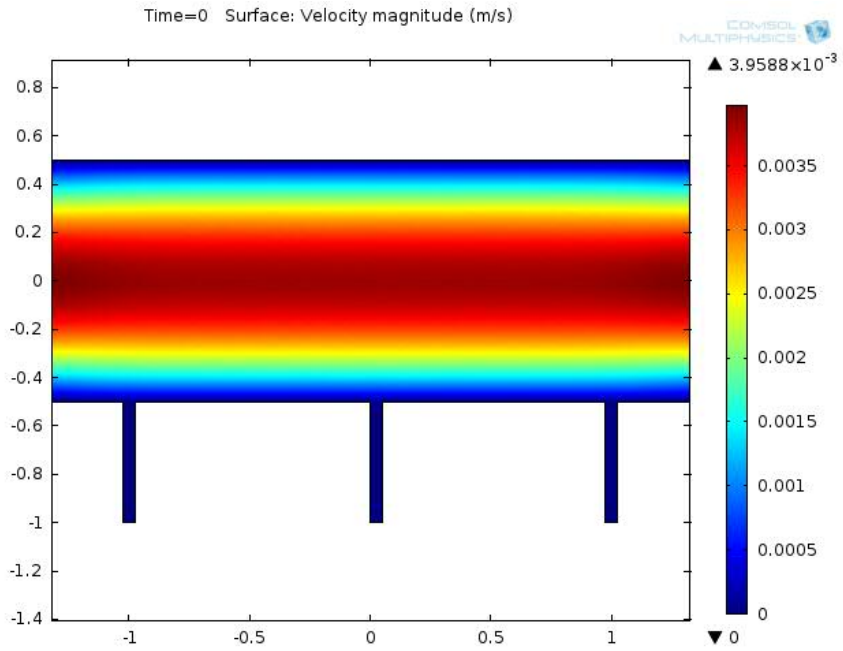

(a) Slice showing velocity profile through an opening dynamic nanochannel sensor.

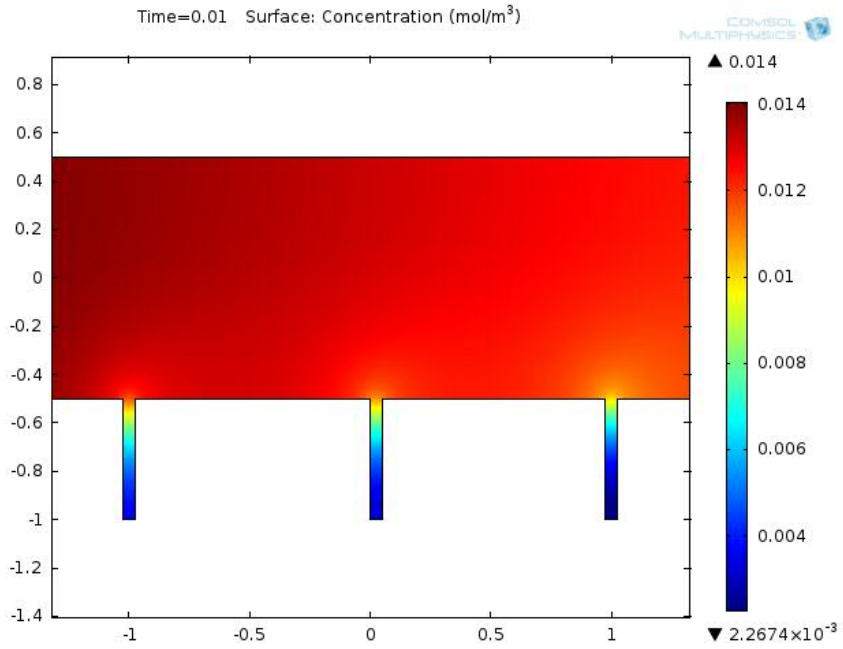

(b) Slice showing concentration densities in the sensor.

Figure 5.1: COMSOL simulations of the velocity profile and concentration profile above the nanochannels.

nanochannels is very high necessitating high pressures to attain substantial volumetric flow rates. Thus the limitation Schoch et al. encountered to higher volumetric flow rates came from the amount pressure their pump was able to supply [23]. If a large volumetric flow rate is attained then the nanochannel dimensions require the fluid passing through the channels to have exceptionally large linear velocities. These velocities mean there will be considerable shear forces on the attached biomolecules, enough even to detach bound protein [23]. These two opposing forces mean there is a flow rate where biomolecular flux will be optimized in static nanochannels. They also limit the quantity of analyte which can be introduced to the nanochannels within a given time period.

The COMSOL Multiphysics simulation platform was used to determine flow rate over the channels and molecular flux to the nanochannel walls (see Fig. 5.1a and Fig. 5.1b). A slice of the nanochannel array sensor with three nanochannels placed under a two micrometer fluidic channel was modeled. The nanochannel walls were given a boundary condition where they would simulate a surface functionalized with binding probabilities given by their respective K_d. The top and bottom of the fluidic channel were given no slip boundary conditions and treated as passivated to the target analyte. Fluid entered on the left with a velocity simulated using the pressure drop across the length of the section and the channel dimensions. The pressure difference used of 90 Pa was calculated by taking the total pressure drop across the length of the fluidic channel divided by the relative length of the simulated section. The center of the flow channel sees the highest flow velocities (in red image Fig. 5.1a). This can be increased to more than 10mm/s with a reasonable channel height (2μm). The nanochannels are not in main flow region, but rest below it. Because of their location in the flow channel many of the target analyte molecules don't interact with the nanochannel sensor walls as they pass the nanochannels. This has a detrimental effect on sample use though recirculation valves could help alleviate this problem. Although dynamic nanochannel sensors use of sample volume is not as efficient as other nanochannel sensors, they keep the nanochannel walls from being exposed to the shear forces from high velocity flow.

Once biomolecules have been transported to the surface of nanochannel walls they must attach to occlude ion transport. The probability of a molecule attaching to a surface

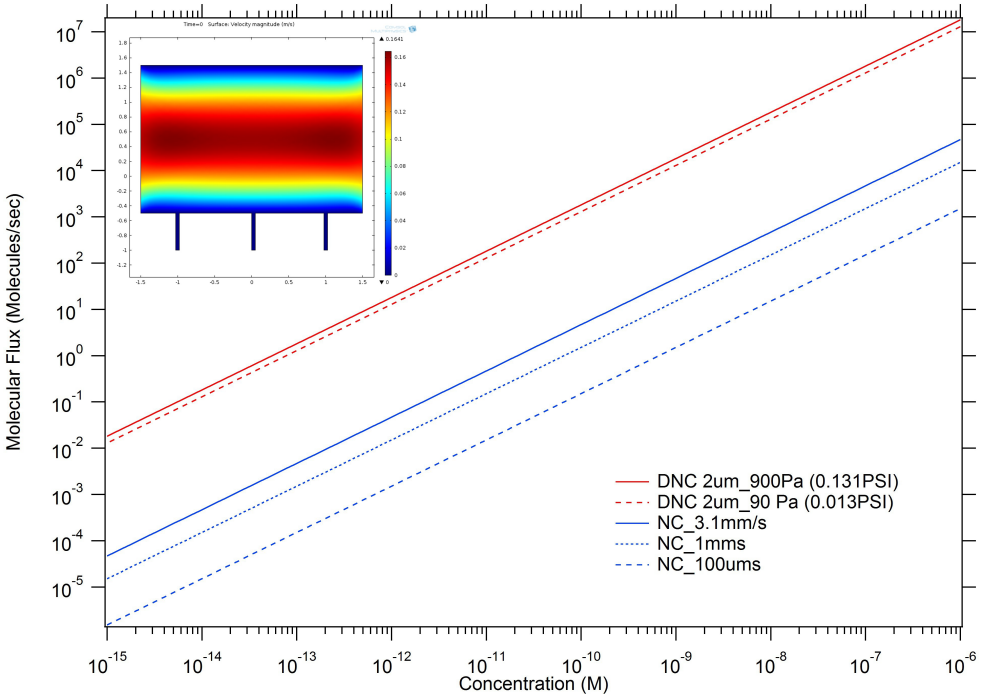

Figure 5.2: Simulated flux to the nanochannel surfaces with dynamic nanochannel sensors versus those reported in literature. Molecular Flux refers to the number of molecules attaching to a single nanochannel.

depends primarily on if the surface has been functionalized for that analyte and the dissociation constant K_d between the receptor and the analyte. The sensor described in the previous chapter depended on non-specific binding which slowed down the reaction time. K_d describes the critical concentration in the fluid at which there will be 50% coverage of the analyte on the sensor walls. This number varies depending on the receptor and analyte chosen. For BSA attaching nonspecifically to quartz the dissociation constant is 200nM; for streptavidin attaching specifically to biotin K_d is 1fM, six orders of magnitude lower and virtually guaranteeing all streptavidin which encounters the biotin attached to the nanochannel walls will bind and remain. Fig. 5.2 shows the simulated flux density to one dynamic nanochannel compared to a static nanochannel sensor. Use of a flow channel situated above the nanochannels allows for greater than a two order of magnitude increase in the number molecules being transported to the nanochannel surfaces. These simulations are in accord with limits described in literature [33].

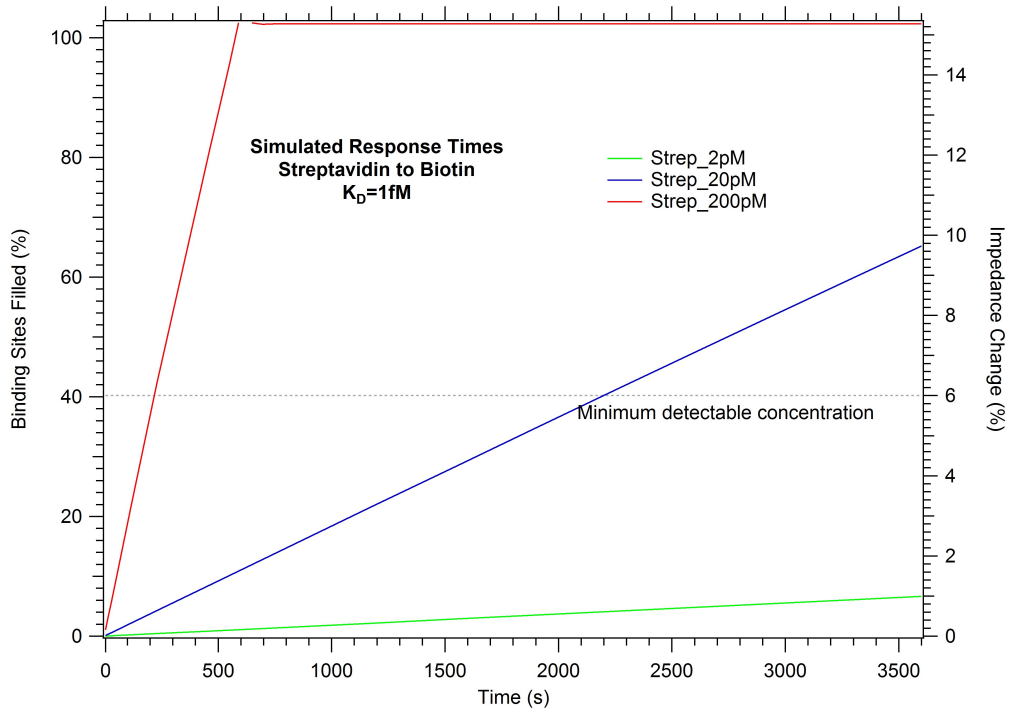

Figure 5.3: Response times with a different K_d this modeling streptavidin binding to biotin attached to the sensor surfaces.

The detection limit of the dynamic nanochannel sensor depends on the number of biomolecules which attach to the sensing surfaces and the sensitivity of the transduction method. Figure 5.3 shows an example of the biomolecules which attach in a single nanochannel using the strong biotin-streptavidin bond in the model. The linear slope of the lines represents the molecular flux density. The valves offer the advantage of increasing the number of molecules which can be attached to the sensor walls in a given time period, but the PDMS valves so far have decreased the sensitivity of the impedance scans relative to static nanochannel sensors because they introduce variability. In Fig. 5.3 the minimum detectable limit is set by taking three times the standard deviation of that variability. This variability comes from the elastomeric PMDS membrane sealing differently between scans. Several factors appear to be influencing this effect. The first is that the valve takes time to seal completely and there is a time delay in the valve sealing to ionic flow. During testing of the sensor in the previous chapter scans were taken 30 seconds after the valves were actuated. However the timing of this process was not automated and therefore inconsistent. The scans were taken over a wide range of frequencies which gave information useful for constructing

an equivalent circuit but increased the time needed per scan. In addition to the time component of the valves closing they are also sensitive to slight variations in the fluid pressure after different fluids have been introduced to the sensor. These variations change the pressure needed to fully close a valve. Finally pieces of debris which would have been removed had we employed an in-chip filter could lodge under the valve affecting its function. These effects worked to decrease the consistency of the valves in our fabricated proof of concept device compared to static nanochannel sensors. However these are not insurmountable challenges. With a valve design more suited to decreasing variations, and more careful control of fluid pressure the variability of the device could be vastly decreased, giving the sensor transduction characteristics more similar to static nanochannel sensors.

Due to the PDMS valves the variability of the device tested in Chapter 3 was higher than desired. Three times the average variability was used as the detection threshold and was equivalent to the change in the impedance signal with about 40% of the available binding sites filled. If the surface was functionalized with biotin and streptavidin was flowed through the channels a 20pM concentration of streptavidin should be detectable in 40 minutes (see Fig. 5.3). This detection limit is due to the high binding affinity of streptavidin to biotin. If the variability of the system was decreased an order of magnitude, which is reasonable with redesigned valves, then a 2pM concentration of streptavidin becomes detectable in 40 minutes. A picomolar concentration is the level given by Diamandis for many biomarker concentrations in serum [5].

Chapter 6

Conclusion

Widespread proteomic biomarker screening has the capability to save thousands of lives a year. Its potential impact in decreasing cancer-related suffering in the United States alone is enormous. Sensitive, inexpensive sensors are key to allowing proteomic biomarkers to realize their potential in these applications. Such sensors should be able to inexpensively detect proteomic biomarkers in picomolar concentrations or less. Impedance spectroscopy sensing is one of the least expensive transduction methods available while providing a straightforward detection model.

Unfortunately, fabricating and testing a dynamic nanochannel sensor was not as straightforward as the conceptual model. During the experiments there were many unexpected roadblocks. Milling nano-trenches turned out to be slow and expensive. It happened that PDMS isn't ideal for impedance sensing. The curing agent used for PDMS to quartz bonding tended to contaminate sensor surfaces while the PDMS-based valves wouldn't easily seal to ionic flow, making consistent impedance measurements difficult. To detect biomolecules as small as proteins we needed the conduction channel to have a critical dimension on the order of tens of nanometers leading to the eventual design of dynamic nanochannel array sensors.

Finally we designed, fabricated, and testing a working dynamic nanochannel sensor. Using PDMS at the limits of its abilities, the control valve closed to ionic flow and we measured protein capture to nanochannel walls. This sensor gave a higher than expected response to non-specifically bound BSA to the nanochannels walls. When opened, the dynamic nanochannel sensors should allow more molecules to bind to nanochannel surfaces compared to static nanochannel designs. This improvement comes due to the much larger microfluidic flow channels of the dynamic nanochannel sensors. With these flow velocities

and sensor geometry the fabricated sensor, if functionalized, should be able to detect protein concentrations in the tens of picomolars.

While several biomarkers present in the concentration range of tens of picomolars there is a clear path to increase the sensitivity of the device even lower. First, the valves should be updated. PDMS is not ideal for dynamic nanochannel sensors due to non-specific binding issues [34], curing agent contamination, out-gassing, and difficulty sealing to ionic flow. A new microfluidic polymer should allow for a valve which will close quicker and more consistently to ionic flow. Improvements with the valve would increase the sensitivity of the device dramatically. Other future work on the dynamic nanochannel sensor array includes developing an E-beam lithography step for patterning the nanochannels to reduce fabrication cost and time. As mentioned in the background chapter, the ratio of the width of the nanochannel to the occluded area of the biomarker determines the impedance change per attached molecule. The widths of the nanochannels could be optimized further by accounting for the relative impedance change for a given biomolecule and its diffusion constant. Developing an amplification step using gold nanoparticles or other similar particles could also drastically increase the sensitivity of the device [27]. After the sensitivity of the dynamic nanochannel arrays has been optimized, functionalizing the arrays for a panel of biomarkers would be the next step. Including many sensors multiplexed on a single chip could then be accomplished. Once the sensors are proven to work with a panel of biomarkers in serum the final step would be to package the sensors with a hand-held or table-top all-in-one measurement device. The beauty of the impedance sensor is that these final steps of multiplexing and packaging should be straightforward.

With these steps completed the dynamic nanochannel would be a powerful and inexpensive tool for widespread biomarker screening allowing vastly improved prognosis for many who suffer.

Bibliography

[1] W. S. Dalton and S. H. Friend, "Cancer biomarkers?an invitation to the table," *Science*, vol. 312, no. 5777, pp. 1165–1168, 2006. [Online]. Available: http://www.sciencemag.org/content/312/5777/1165.abstract 1, 2

[2] C. L. Sawyers, "The cancer biomarker problem," *Nature*, vol. 452, pp. 548–552, March 2008. [Online]. Available: http://www.nature.com/nature/journal/v452/n7187/abs/nature06913.html 1, 2

[3] R. Etzioni, N. Urban, S. Ramsey, M. McIntosh, S. Schwartz, B. Reid, J. Radich, G. Anderson, and L. Hartwell, "The case for early detection," *Nat Rev Cancer*, vol. 3, pp. 243–252, 2003. [Online]. Available: http://dx.doi.org/10.1038/nrc1041 1

[4] R. J. Simpson, O. K. Bernhard, D. W. Greening, and R. L. Moritz, "Proteomics-driven cancer biomarker discovery: looking to the future," *Current Opinion in Chemical Biology*, vol. 12, no. 1, pp. 72 – 77, 2008. [Online]. Available: http://www.sciencedirect.com/science/article/pii/S1367593108000379 1

[5] E. P. Diamandis, "Mass spectrometry as a diagnostic and a cancer biomarker discovery tool: Opportunities and potential limitations," *Molecular & Cellular Proteomics*, vol. 3, no. 4, pp. 367–378, 2004. [Online]. Available: http://www.mcponline.org/content/3/4/367.abstract 1, 49

[6] B. L. Zybailov and M. P. Washburn, *Mass Spectrometry-based Methods of Proteome Analysis*. Wiley-VCH Verlag GmbH & Co. KGaA, 2006. [Online]. Available: http://dx.doi.org/10.1002/3527600906.mcb.200400028 1

[7] M. Polanski and N. L. Anderson, "A list of candidate cancer biomarkers for targeted proteomics," *Biomarker Insights*, vol. 1, pp. 1–48, 02 2007. [Online]. Available: www.la-press.com/a-list-of-candidate-cancer-biomarkers-for-targeted-proteomics-article-a29 1, 2

[8] A. C. Society, "Cancer facts & figures 2013," http://www.cancer.org/Research/CancerFactsFigures/CancerFactsFigures/2013-cancer-facts-and-figures.pdf, 2013. [Online]. Available: http://www.cancer.org/Research/CancerFactsFigures/CancerFactsFigures/2013-cancer-facts-and-figures.pdf 1

[9] B. Laxman, D. S. Morris, J. Yu, J. Siddiqui, J. Cao, R. Mehra, R. J. Lonigro, A. Tsodikov, J. T. Wei, S. A. Tomlins, and A. M. Chinnaiyan, "A first-generation multiplex biomarker analysis of urine for the early detection of prostate

cancer," *Cancer Research*, vol. 68, no. 3, pp. 645–649, 2008. [Online]. Available: http://cancerres.aacrjournals.org/content/68/3/645.abstract 2

[10] K. R. Kozak, F. Su, J. P. Whitelegge, K. Faull, S. Reddy, and R. Farias-Eisner, "Characterization of serum biomarkers for detection of early stage ovarian cancer," *PROTEOMICS*, vol. 5, no. 17, pp. 4589–4596, 2005. [Online]. Available: http://dx.doi.org/10.1002/pmic.200500093 2

[11] S. Ness, R. Anderson, W. Hu, D. Richards, J. Oxborrow, T. Gustafson, B. Tsai, S. Kim, B. Mazzeo, A. Woolley, and G. Nordin, "Weak adsorption-induced surface stress for streptavidin binding to biotin tethered to silicon microcantilever arrays," *Sensors Journal, IEEE*, vol. 13, no. 3, pp. 959–968, 2013. 2

[12] J. Kasianowicz, E. Brandin, D. Branton, and D. Deamer, "Characterization of individual polynucleotide molecules using a membranechannel," *Proceedings of the National Academy of Sciences*, vol. 93, no. 24, pp. 13 770–13 773, 1996. [Online]. Available: http://www.pnas.org/content/93/24/13770.abstract 4

[13] O. A. Saleh and L. L. Sohn, "An artificial nanopore for molecular sensing," *Nano Letters*, vol. 3, no. 1, pp. 37–38, 2003. [Online]. Available: http://pubs.acs.org/doi/abs/10.1021/nl0255202 4

[14] H. Chang, F. Kosari, G. Andreadakis, M. A. Alam, G. Vasmatzis, and R. Bashir, "Dna-mediated fluctuations in ionic current through silicon oxide nanopore channels," *Nano Letters*, vol. 4, no. 8, pp. 1551–1556, 2004. [Online]. Available: http://pubs.acs.org/doi/abs/10.1021/nl049267c 4

[15] Y. Kim, J. Min, I. Lee, S. Kim, A. Kim, K. Kim, K. Namkoong, and C. Ko, "Nanopore sensor for fast label-free detection of short double-stranded {DNAs}," *Biosensors and Bioelectronics*, vol. 22, no. 12, pp. 2926 – 2931, 2007, ¡ce:title¿Chem and Biosensing Transistors: from materials to systems¡/ce:title¿. [Online]. Available: http://www.sciencedirect.com/science/article/pii/S095656630600577X 4

[16] D. Branton, D. W. Deamer, A. Marziali, H. Bayley, S. A. Benner, T. Butler, M. Di Ventra, S. Garaj, A. Hibbs, X. Huang, S. B. Jovanovich, P. S. Krstic, S. Lindsay, X. S. Ling, C. H. Mastrangelo, A. Meller, J. S. Oliver, Y. V. Pershin, J. M. Ramsey, R. Riehn, G. V. Soni, V. Tabard-Cossa, M. Wanunu, M. Wiggin, and J. A. Schloss, "The potential and challenges of nanopore sequencing," *Nat Biotech*, vol. 26, pp. 1146–1153, 2008. [Online]. Available: http://dx.doi.org/10.1038/nbt.1495 4, 5

[17] H. T. Hoang, I. M. Segers-Nolten, J. W. Berenschot, M. J. de Boer, N. R. Tas, J. Haneveld, and M. C. Elwenspoek, "Fabrication and interfacing of nanochannel devices for single-molecule studies," *Journal of Micromechanics and Microengineering*, vol. 19, no. 6, p. 065017, 2009. [Online]. Available: http://stacks.iop.org/0960-1317/19/i=6/a=065017 4

[18] M. Ventra, M. Krems, J. Wilson, and Y. Pershin, "Dna characterization by transverse electrical current in a nanochannel," *Methods in Molecular Biology*, vol. 870, pp. 149–163, 2012. [Online]. Available: http://www.ncbi.nlm.nih.gov/pubmed/22528263 4

[19] P. V. Gerwen, W. Laureyn, W. Laureys, G. Huyberechts, M. O. D. Beeck, K. Baert, J. Suls, W. Sansen, P. Jacobs, L. Hermans, and R. Mertens, "Nanoscaled interdigitated electrode arrays for biochemical sensors," *Sensors and Actuators B: Chemical*, vol. 49, no. 12, pp. 73 – 80, 1998. [Online]. Available: http://www.sciencedirect.com/science/article/pii/S0925400598001282 4, 9

[20] R. Karnik, K. Castelino, R. Fan, P. Yang, and A. Majumdar, "Effects of biological reactions and modifications on conductance of nanofluidic channels," *Nano Letters*, vol. 5, no. 9, pp. 1638–1642, 2005. [Online]. Available: http://pubs.acs.org/doi/abs/10.1021/nl050966e 5

[21] N. F. Durand, C. Dellagiacoma, R. Goetschmann, A. Bertsch, I. Marki, T. Lasser, and P. Renaud, "Direct observation of transitions between surface-dominated and bulk diffusion regimes in nanochannels," *Analytical Chemistry*, vol. 81, no. 13, pp. 5407–5412, 2009. [Online]. Available: http://pubs.acs.org/doi/abs/10.1021/ac900617b 5

[22] D. Stein, M. Kruithof, and C. Dekker, "Surface-charge-governed ion transport in nanofluidic channels," *Phys. Rev. Lett.*, vol. 93, p. 035901, Jul 2004. [Online]. Available: http://link.aps.org/doi/10.1103/PhysRevLett.93.035901 5, 42

[23] R. B. Schoch, L. F. Cheow, and J. Han, "Electrical detection of fast reaction kinetics in nanochannels with an induced flow," *Nano Letters*, vol. 7, no. 12, pp. 3895–3900, 2007. [Online]. Available: http://pubs.acs.org/doi/abs/10.1021/nl0724788 5, 6, 44, 46

[24] N. Durand and P. Renaud, "Label-free determination of proteinsurface interaction kinetics by ionic conductance inside a nanochannel," *Lab on a Chip / Virtual Journal of Nanoscale Science & Technology*, vol. 19, no. 3, pp. –, 2009. 6

[25] A. Afanasiev, I. Lhdesmki, and B. Parviz, "Fabrication and electrical characterization of integrated nano-scale fluidic channels," *Microsystem Technologies*, vol. 17, pp. 1511–1518, 2011, 10.1007/s00542-011-1320-0. [Online]. Available: http://dx.doi.org/10.1007/s00542-011-1320-0 6

[26] M. Ali, B. Schiedt, R. Neumann, and W. Ensinger, "Biosensing with functionalized single asymmetric polymer nanochannels," *Macromolecular Bioscience*, vol. 10, no. 1, pp. 28–32, 2010. [Online]. Available: http://dx.doi.org/10.1002/mabi.200900198 6

[27] A. de la Escosura-Muiz and A. Merkoi, "A nanochannel/nanoparticle-based filtering and sensing platform for direct detection of a cancer biomarker in blood," *Small*, vol. 7, no. 5, pp. 675–682, 2011. [Online]. Available: http://dx.doi.org/10.1002/smll.201002349 6, 51

[28] F. Zhang, M. W. A. Skoda, R. M. J. Jacobs, R. A. Martin, C. M. Martin, and F. Schreiber, "Protein interactions studied by saxs: Effect of ionic strength and protein concentration for bsa in aqueous solutions," *The Journal of Physical Chemistry B*, vol. 111, no. 1, pp. 251–259, 2007, pMID: 17201449. [Online]. Available: http://pubs.acs.org/doi/abs/10.1021/jp0649955 8, 42

[29] L. Tsai, W. C. Dahlquist, S. Kim, and G. P. Nordin, "Bonding of polydimethylsiloxane microfluidics to silicon-based sensors," *Journal of Micro/Nanolithography, MEMS, and MOEMS*, vol. 10, no. 4, pp. 043 009–043 009–8, 2011. [Online]. Available: +http://dx.doi.org/10.1117/1.3659139 13, 39

[30] Z. Zou, S. Lee, and C. H. Ahn, "A polymer microfluidic chip with interdigitated electrodes arrays for simultaneous dielectrophoretic manipulation and impedimetric detection of microparticles," *Sensors Journal, IEEE*, vol. 8, no. 5, pp. 527–535, 2008. [Online]. Available: http://ieeexplore.ieee.org/xpls/icp.jsp?arnumber=4529161 15

[31] M. J. C. Audrey M. Johnson, Donald R. Sadoway and R. Langer, "Design and testing of an impedance-based sensor for monitoring drug delivery," *Journal of the Electrochemical Society*, vol. 152, 2004. [Online]. Available: http://jes.ecsdl.org/content/152/1/H6.full 41

[32] N. A. Mortensen, F. Okkels, and H. Bruus, "Reexamination of hagen-poiseuille flow: Shape dependence of the hydraulic resistance in microchannels," *Phys. Rev. E*, vol. 71, p. 057301, May 2005. [Online]. Available: http://link.aps.org/doi/10.1103/PhysRevE.71.057301 44

[33] P. E. Sheehan and L. J. Whitman, "Detection limits for nanoscale biosensors," *Nano Letters*, vol. 5, no. 4, pp. 803–807, 2005. [Online]. Available: http://pubs.acs.org/doi/abs/10.1021/nl050298x 47

[34] B. Huang, H. Wu, S. Kim, and R. N. Zare, "Coating of poly (dimethylsiloxane) with n-dodecyl-β-d-maltoside to minimize nonspecific protein adsorption," *Lab Chip*, vol. 5, no. 10, pp. 1005–1007, 2005. [Online]. Available: https://www.stanford.edu/group/Zarelab/publinks/756.pdf 51